universität wien

MASTERARBEIT / MASTER'S THESIS

Titel der Masterarbeit / Title of the Master's Thesis

„Structure – composition relation in the Sb-Te system“

verfasst von / submitted by

Stefan Solé B.Sc.

angestrebter akademischer Grad / in partial fulfilment of the requirements for the degree of

Master of Science (M.Sc.)

Wien, 2018 / Vienna 2018

Studienkennzahl lt. Studienblatt / degree programme code as it appears on the student record sheet:	A 066 862
Studienrichtung lt. Studienblatt / degree programme as it appears on the student record sheet:	Masterstudium Chemie
Betreut von / Supervisor:	ao. Univ.-Prof. Mag. Dr. Klaus Richter

Acknowledgements

In the following I want to thank all people, who helped and contributed to this master thesis.

For giving me the opportunity to work on this interesting topic, valuable insights and assistance whenever needed, I want to first and foremost thank ao. Univ.-Prof. Mag. Dr. Klaus Richter.

I want to express special gratitude to Dr. Clemens Schmetterer for his guidance on certain, nontrivial issues and for his patience, while explaining. Also, I want to thank all other colleagues of the working group.

Special thanks go to Dr. Stephan Puchegger of the Faculty Center for Nanostructure Research for his support whilst the SEM measurements.

Lastly, I want the thank my family and friends for their implicit support.

Table of content

List of Figures

List of tables

1. Introduction

Due to the importance of semiconductors and phase change materials, which are both needed for modern technological applications, various materials have been investigated since the mid-20th century. Intermetallic Sb-Te alloys have been receiving quite much attention in the last years due to them having various interesting properties. When doped with a suitable dopant Sb_2Te_3 can be transformed into both p-type and n-type semiconductors [1]. It can be used as phase change material for random access memory, when Germanium and Indium are added [2], or as base material for optical disc memory [3].

Also, reports of Sb-Te being a topological insulator (a material which behaves like an insulator in the bulk but also allows load carrying on the surface), is frequently found in literature [4-6].

Due to the various useful properties many different studies have already been made on this phase diagram since the early 20th century. Whereas the first studies were mostly thermal analysis [7, 8], later researchers also provided structure analysis and computerized assessed phase diagram assessments utilizing for instance the CALPHAD method (calculation of phase diagrams) [9-11]. Nevertheless, there is no agreement on the equilibrium phase diagram, since different studies contradict each other.

Aim of this work was the reinvestigation of the Sb-rich part of the Sb-Te phase diagram based on the work given by Ghosh et al. [12]. Several samples were prepared with steadily increasing Te percentage, starting from 6 at.% Te to 50 at% in 2 at.% steps plus various samples from 50 to 60 at.% without defined order. All samples were examined utilizing X-ray powder diffraction, differential thermal analysis, optical microscopy, scanning electron microscopy and electron probe microanalysis. The structures of the samples were investigated using Rietveld refinement and compared with existing literature data.

Finally, a revised phase diagram could be developed, based on the obtained results.

2. Basic materials overviews

2.1 Sb

Antimony, even though not being abundant, can be found in various mineral species with the sulfide stibnite (Sb_2S_3) being the most frequently found. The pure metal can be obtained in the process of high quality stibnite reacting with iron scraps at a temperature where stibnite is melted. On the other hand, when low quality ores are used it is first roasted to the antimony oxide (Sb_2O_3). The product is further treated with thermal reduction with carbon to obtain the pure metal [13].

Although being stable at room temperature, it reacts with oxygen at elevated temperatures to antimony trioxide. Antimony, a silver-grey metal with a Mohs hardness of 3, crystallises with the trigonal layered structure (space group 166; *R*-3*m*) of the As-type. The close packing of antimony leads to the relatively high density, while the weak bonding between the layers is responsible for the low Mohs hardness and its brittleness. Antimony is a poor conductor for heat and electricity and is not affected by diluted alkaline solutions or acids. Other than most metals antimony has a relatively high vapor pressure being 1 atm at 1587°C [14, 15].

Atomic number	51
Electron configuration	[Kr] $4s^2$ $3d^{10}$ $4p^3$
Classification	15^{th}, pnictogen
Atomic mass [g/mol-1]	121.76
Covalent radius [pm]	145
Melting point [°C]	630.63
Density [g/m³]	6.70

Table 2.1: Properties of Antimony [16].

2.2 Te

Tellurium, a very rare element in the earth's crust comparable to platinum is mostly found in tellurium containing compounds like gold chalcogenides. Nevertheless, most tellurium is extracted as a by-product during the production of copper or lead. The main source is from anode sludges generated while the electrolytic refinement of copper. The sludges contain the noble metal tellurides with the general formula Me_2Te (M = Cu, Ag, Au). The anode sludges are roasted under air with sodium carbonate at elevated temperatures of 500°C. The noble metals are reduced, while sodium telluride is generated (Na_2TeO_3). In alkaline milieu sodium telluride reacts to the insoluble species tellurium oxide (TeO_2). The tellurium metal is produced via electrolysis or by reacting with SO_2 in sulfuric acid [13].

Tellurium is a silver, very brittle, easily pulverized metal with a Mohs hardness of 2.25. It is a semiconductor with greater conductivity, depending on atomic alignment, in certain directions [17]. Tellurium crystallises like antimony trigonal (space group 154; $P3_221$) and like antimony, tellurium has a relatively high vapor pressure of 1 atm at 988°C [14, 15].

Atomic number	52
Electron configuration	[Kr] $4s^2$ $3d^{10}$ $4p^4$
Classification	16^{th}, chalcogen
Atomic mass [g/mol-1]	127.6
Covalent radius [pm]	140
Melsting point [°C]	449.51
Density [g/m³]	6.24

Table 2.2: Properties of Tellurium [18].

3. Literature review

3.1 Literature available on the Sb-Te system

There exists various different literature on the Sb-Te phase diagram, some of them disagreeing with each other. The region between pure Sb and the Sb_2Te_3 phase is of special interest, because phase equilibria in the area are poorly understood and discussed controversially.

This thesis is based on the calculated phase diagram by Ghosh et al. [12].

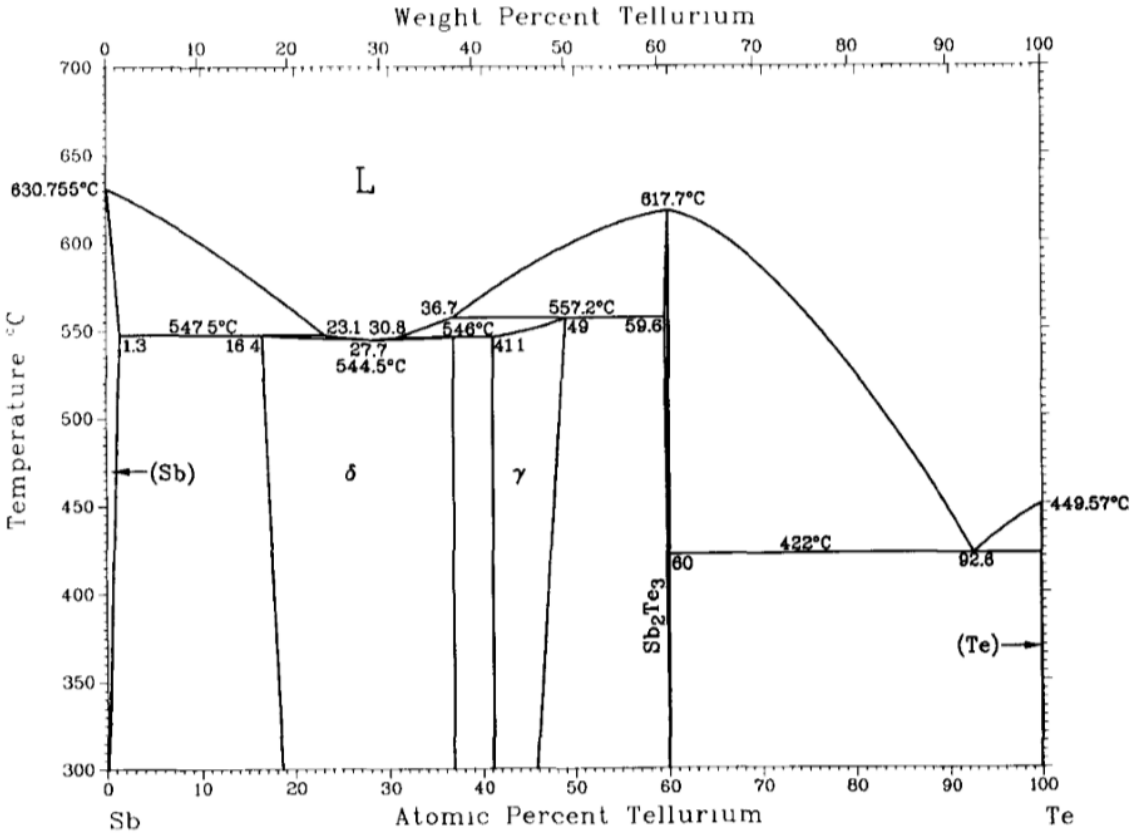

Figure 3.1: Calculated phase diagram by Ghosh et at. [12].

The phase diagram is shown in figure 3.1. Between 0 and 60 at.% Te the phase diagram shows three peritectic reactions, in a very close temperature range. The peritectic reactions at 16.4 at.% Te (T = 547.5°C) and at 36.8 at.% Te (T = 546°C) are separated by a congruent melting point (minimum) at 27.7 at.% Te (T = 544.5°C), where a phase transition from the liquid phase to the δ – phase occurs. The last peritectic reaction is located at 49 at.% Te (T = 557.2°C). An overview of

all occurring reactions is given in table 3.1. Ghosh at. al. stated in his work that there are 2 separated phases δ and γ. Between pure Sb, which has a solubility of Te up to 1.3 at.%, and the δ-phase we have a two phase field going from 1.3 to 16.4 at.% Te. This two phase field is followed by the broad single phase field of δ, which is spread from 16.4 at.% Te to 36.8 at.% Te. Between the δ and γ phases is a small two phase field followed by the γ – phase (41.1 to 49 at.% Te). The phase diagram is completed by the congruent melting phase Sb_2Te_3 followed by the eutectic reaction L ↔ Sb_2Te_3 + Te at 92 at.% Te.

Reaction	Composition of the respective phases [at.% Te]			Temperature [°C]	Reaction type
L ↔ Sb		0		630.75	Melting
L + (Sb) ↔ δ	23.1	1.3	16.4	547.35	Peritectic
L ↔ δ	27.7	27.7		544.35	Congruent
L + γ ↔ δ	30.8	41.1	36.7	545.85	Peritectic
L + Sb_2Te_3 ↔ γ	36.7	59.6	49	557.05	Peritectic
L ↔ Sb_2Te_3 + (Te)	92.6	60	100	544.35	Eutectic
L ↔ Te		100		449.55	Melting

Table 3.1: overview of reactions occurring according to Ghosh et al. [12].

The phases δ and γ were constructed by single crystal measurements done in previous works [19 - 21]. It was concluded that δ has a trigonal crystal structure with the space group P-3m1 and the γ phase also a trigonal crystal structure with the space group R-3m. The reported lattice parameters are shown in table 3.2.

Phase	composition [at.% Te]	Space group	Lattice parameter	
			a [Å]	c [Å]
δ	33.3	P-3m1	4.26	17.58
γ	42.86	R-3m	4.25	41.55
	50	R-3m	4.26	23.9

Table 3.2: Lattice parameter found by single crystal studies [19 – 21].

There is more literature supporting the hypothesis of this type of phase diagram construction. Examples would be the works of Abrikosov et al. [22] and Shelomova et al. [23]. There are only minor differences between the phase diagram from Abrikosov et al., which is seen in figure 3.3, and the diagram by Ghosh et al. For instance, the reaction temperatures are varying a bit (e.g. the congruent melting minimum lies at 538°C opposed to 544.5°C) and the γ phase has a broader range (~42 to 55 at.% Te) in Abrikosovs work.

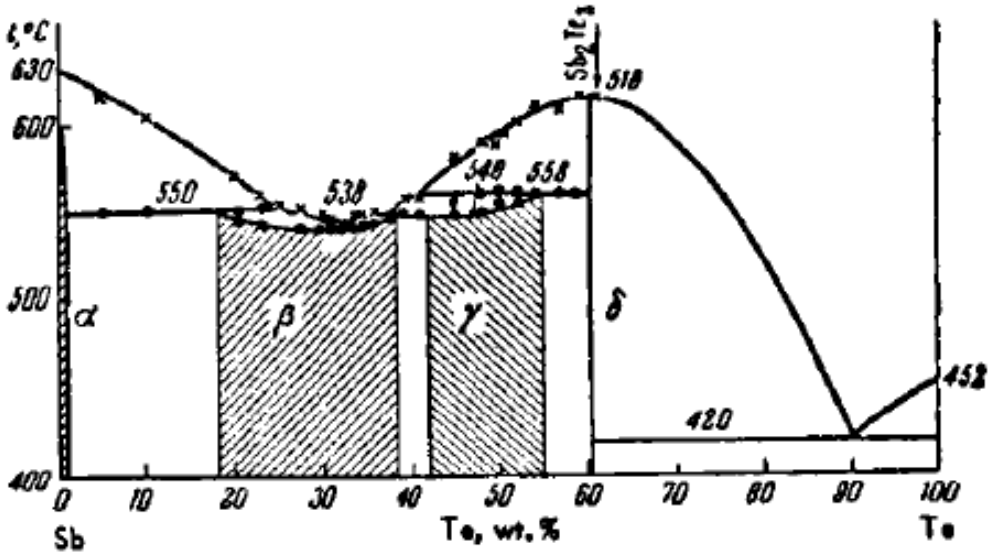

Figure 3.2: Phase diagram given by Abrikosov et al. [22].

The later work of Shelomova et al. [23] is introducing the idea of a homologous series of layered compounds in the Sb-Te system, based on the phase diagram by Ghosh et al. Some of the compounds were prepared in this work, others were taken from literature. The phase diagram can be seen in figure 3.4 and a summary of the layered Sb-Te structures can be found in table 3.3.

Compound	Lattice parameter		Procedure	Source
	a [Å]	c [Å]		
$Sb_{14}Te_6$	4.29	116.39	calculation	[25]
Sb_2Te	4.26	17.8	melt cooling at 5°C/h, annealing at 300°C for 1000h	[23, 21]
$Sb_{10}Te_6$	-	9.481	annealing at 300°C for 1000h	[23]
Sb_4Te_3	4.26	41.55	zone melting	[25]
Sb_6Te_5	4.28	65.06	calculation	[25]
Sb_8Te_7	4.28	88.83	calculation	[25]
Sb_2Te_2	4.26	23.9	zone melting	[20]
Sb_8Te_9	4.27	101.33	calculation	[25]
Sb_4Te_5	4.27	53.79	calculation	[25]

Table 3.3: Summarization of the Sb-Te compounds elaborated by Shelmova et al. [23].

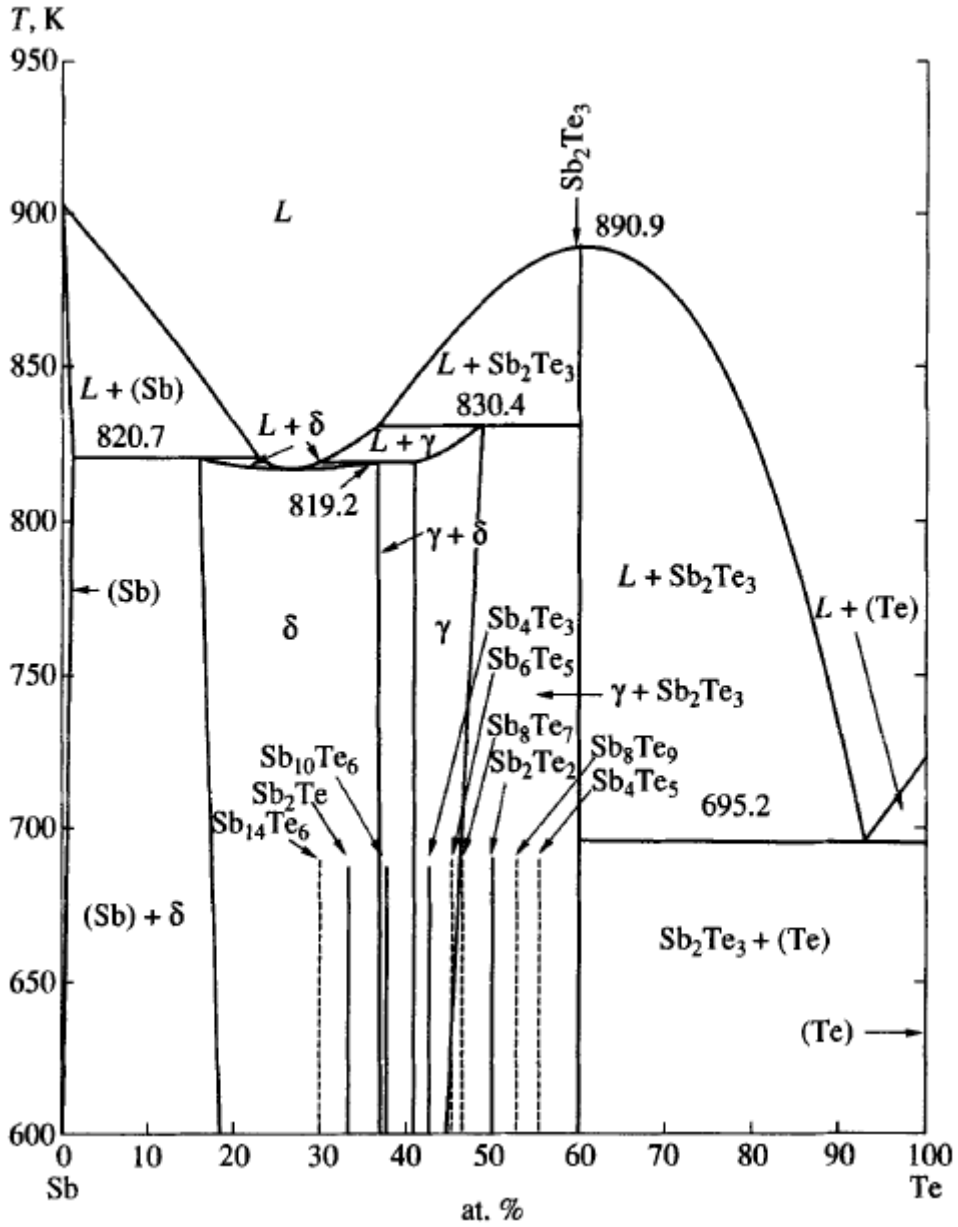

Figure 3.3: Phase diagram by Shelomova et al. [23]. The layered compounds are marked by the vertical full and dashed lines.

Also, the work by Eckerlin and Stegherr [10] concludes to confirm the phase diagram by Abrikosov, but points out that only one peritectic reaction could be verified between 30 at.% Te and Sb_2Te_3. Furthermore, the described γ phase could not be verified and it is stated that there are least 11 discrete phases in this range.

Other literature is showing a different concept regarding the Sb-Te phase diagram. In the work from Brown and Lewis [26] they feature a different phase diagram, where only one broad single-phase field exists between Sb and Sb_2Te_3, going from 11 to 60 at.% Te. The diagram can be seen in figure 3.4.

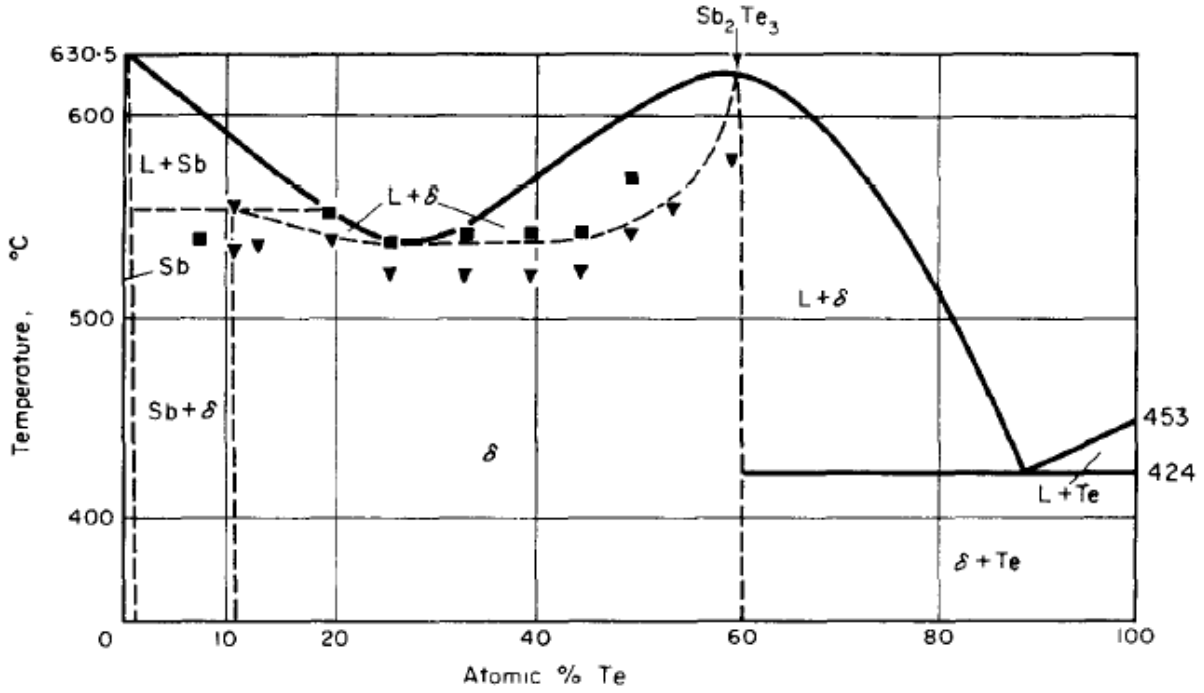

Figure 3.4: Phase diagram by Brown and Lewis [26].

Furthermore, they only verify one peritectic reaction (L + (Sb) ↔ δ) at ~ 550°C. Their results were combined with results quoted from previous work done by Hansen and Anderko [27] to yield the shape of the liquidus and therefore providing the phase diagram in its pictured shape. In their work, Brown and Lewis suggest that that the two distinct phases found by Abrikosov et al. could be metastable compounds [26].

A later work by Kim and Chao reinvestigates especially the liquidus and solidus in the range from Sb to Sb_2Te_3. They introduce furthermore, through electron microprobe analysis, a wide range of compositions between 20 and 60 at.% Te. They conclude that the below solidus temperature remains uncertain, in said range, and that prior work, with two different single-phase fields cannot be approved [28]. Their phase diagram suggestion is given in figure 3.5 and their thermal analysis data in table 3.4.

The concept of layered structures was also further investigated in following thin film deposition studies by Kifune at al. [11, 29], where also only one intermediate single-phase field exists.

Composition [at.% Te]	Peaks [°C]
5.18	549
	616
14.91	547
	583
20.08	544
	549
25.03	544.8
34.97	545
40.25	544
44.92	544
	567
49.9	544
	585
56.86	539
	618.5

Table 3.4: Differential thermal analysis data by Kim and Chao [28].

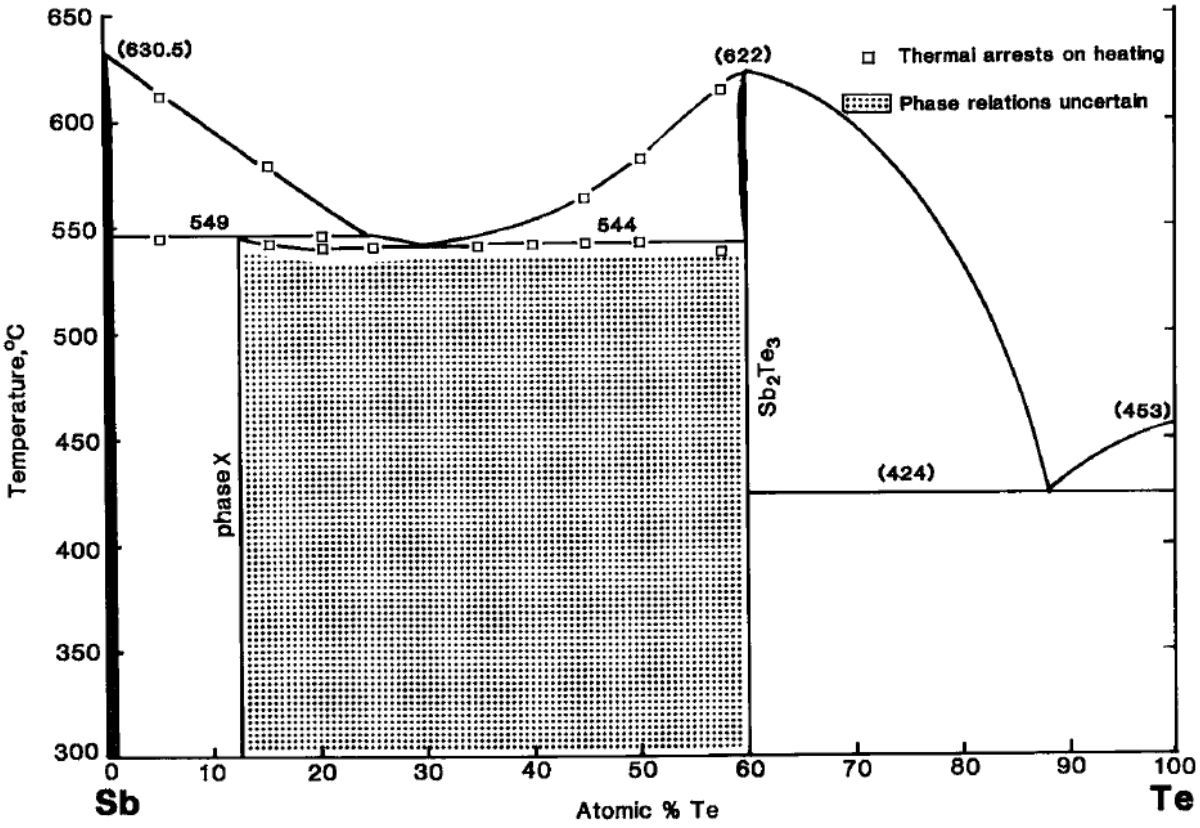

Figure 3.5: Phase diagram suggestion by Kim and Chao [28].

3.2 Correlation of different crystal structures from Sb to Sb_2Te_3

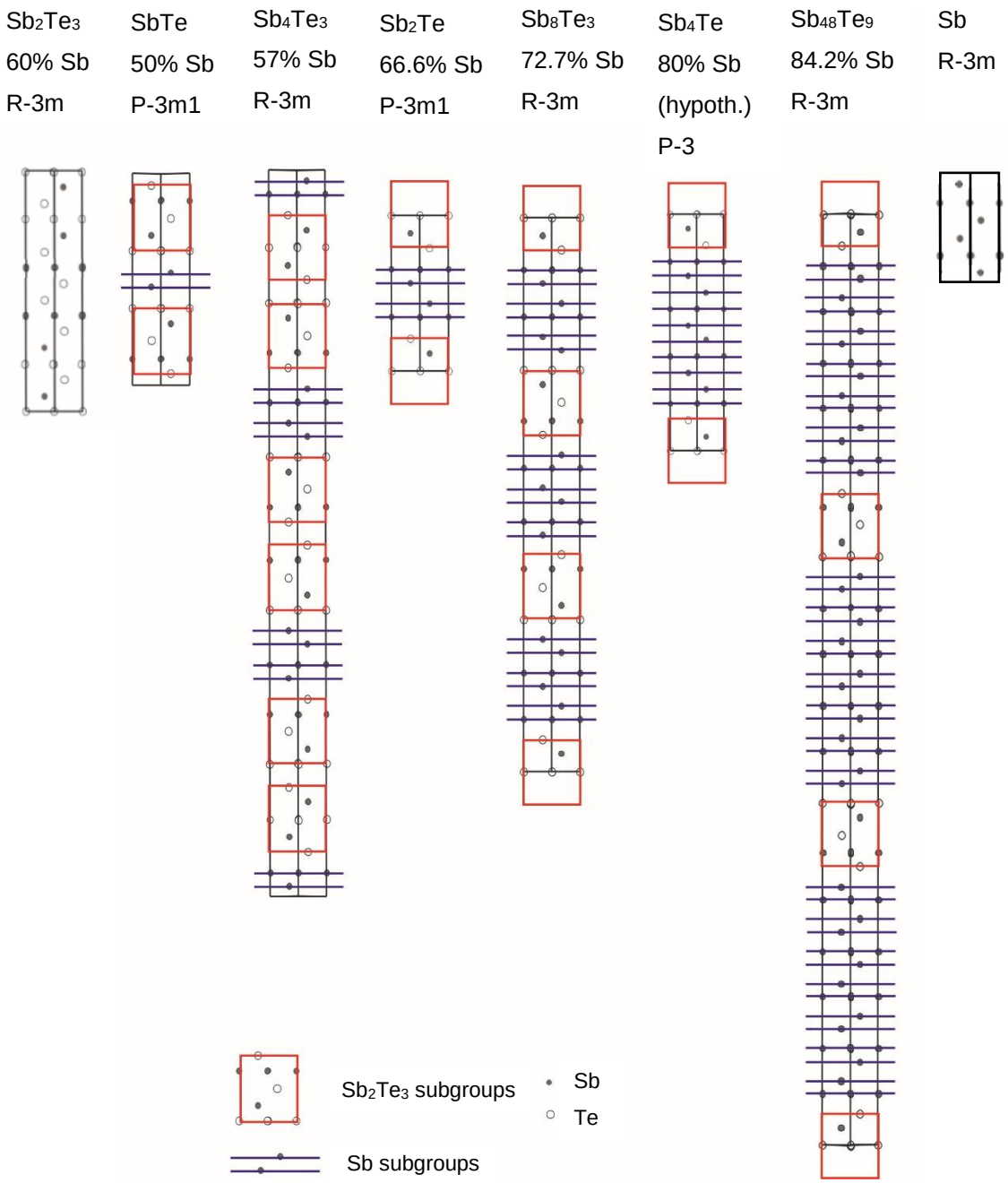

Figure 3.6: Unit cells of all refined structures in comparison to the unit cells of the subgroups Sb and Sb_2Te_3.

Figure 3.6 shows all refined structures, which are built upon on Sb_2Te_3 and Sb_2 subgroups. All structures are based on the As-structure type and therefore possessing a trigonal unit cell. All shown structures are R-centered, with the two exceptions Sb_2Te and Sb_4Te, which are both having a primitive superstructure.

3.3 Commensurate and incommensurate modulated structures

The normally observed commensurate structures are based on the base concept in crystallography, the lattice periodicity. To be able to fully describe crystallized matter this trait is assumed to be crucial. Nevertheless, condensed matter not having lattice periodicity has been discovered over the last decades. These long range ordered phases differ only in very minor physical and structural characteristics, which are difficult to detect.

The terminus modulated used in the headline can be described as a deformation of the crystal structure, occurring periodically. A modulated crystal structure is referred to as incommensurate, when the periodical deformation doesn't belong to the crystal structure. This description can be visually observed, when evaluating a diffraction pattern. In the vicinity of main reflections additional reflections can be seen, which have in general weaker intensity. These supplementary reflections are called satellites and can be seen in figure 3.6. It was

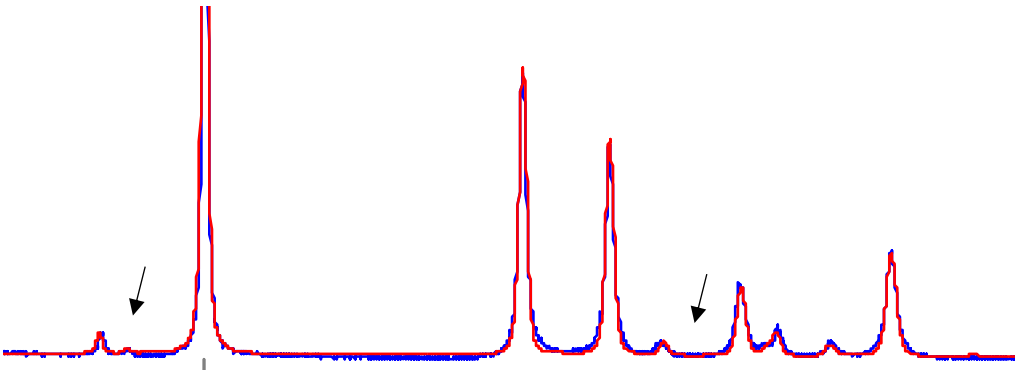

Figure 3.7: Satellites (weak reflections) next to prominent reflections.

shown by Donnay that additional reflections in diffraction pattern correspond to not indexable faces, while studying calverite crystals [30].

Main reflections can be labelled as h, k and l. The satellites are distinct from the main reflections by a modulation vector, which can be described as q_j (j=1, 2, …d). In this study d=1, since the crystal structures are one-dimensional modulated (in direction of the c-axis).

If no lattice can be formed with a given set of positions, then an incommensurate modulation occurs. This modulation, which is liable for the occurrence of satellites can either be a displacive- or an occupation modulation.

The former one can be described as a periodic displacement of atomic positions, while in the latter one, an atomic position of the basic structure can be occupied under the rules of a periodic probability function. There are also occurring mixed forms or even other types of modulations. Korekawa studied the satellite reflections in respect of the various different types of modulations [31]. A crystal structure can be classified as incommensurate, when of the modulation wavevector q_j at the very least one component is irrational, in respect of the main lattice reflections [32].

4. Theoretical background

4.1 Phase Diagrams

A phase diagram describes graphically the state of a system, containing one or more compounds in thermodynamic equilibrium, as a function of temperature, pressure and composition. A phase is a homogeneous representation of a state of matter described by composition a chemical structure. An example of a phase would be the solid, liquid and gaseous state of a material in a unary phase diagram. A unary phase diagram is a graphical representation of one element. If more elements are added binary, ternary or even higher order phase diagram are developed. The higher ordered diagrams show the direct relation of elements and compounds under equilibrium conditions in form of phase fields. This leads to a so-called heterogeneous equilibrium, where distinct phases are in thermodynamic equilibrium. When thermodynamic equilibrium is achieved, the Gibb's free energy is at a minimum.

$$(G)_{T,\ p,\ x1,\ldots xi} = \min$$

Therefore, metastable conditions are normally not represented, except for a few cases. For instance, the metastable compound cementite (Fe_3C) is insert in the Fe-C phase diagram for technological reasons [33].

Phase diagrams yield many essential information for technical applications, for instance soldering, contacting of semiconductors and welding and are the basis of understanding and predicting material properties.

To properly read phase diagrams, certain rules must be considered. All rules are valid for binary and higher ordered phase diagrams. The most important rule is the Gibb's phase rule:

$$p + f = c + 2$$

If we consider that the pressure in condensed systems has often no significant effect on the equilibrium (p = constant) we can derive the following phase rule

$$p + f' = c + 1$$

p number of phases

c number of components

f degrees of freedom

If one wants to construct a phase diagram the rule of Landau and Palatnik is indispensable. It is expressed as

$$r_1 = r - d^- - d^+$$

where r_1 is the dimension of the border, r the phase diagram dimension and d^- d^+ stand for the number of phases lost and added through the phase field transition.

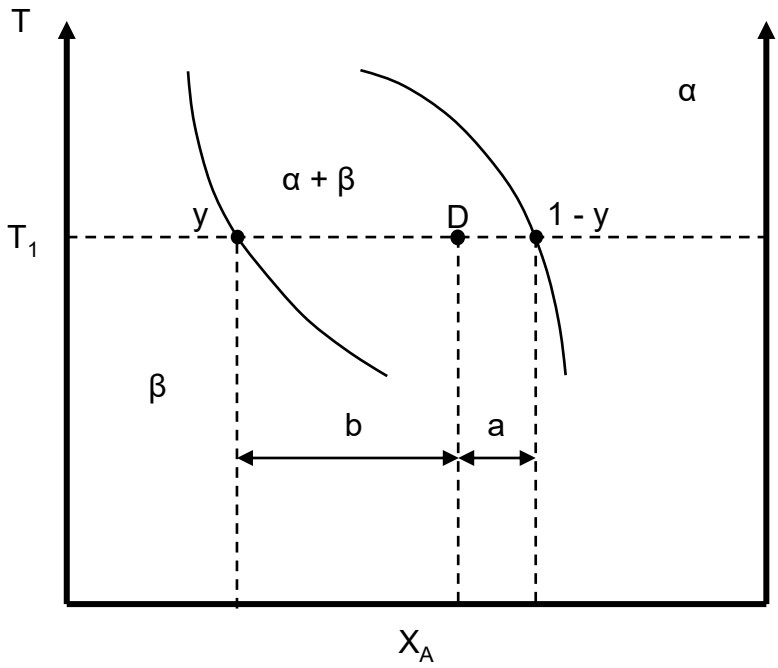

Figure 4.1: Visualization of the Lever rule.

Another valuable tool needed to work with phase diagrams is the Lever rule. Figure 4.1 shows two phases α and β, which are separated by a two-phase field containing α+ β. In the example we have a sample with the composition D, located in the two-phase field, at a certain temperature T_1. The two single phases are connected through a horizontal line called tie line, which describes the equilibrium between both phases at the given temperature. With the Lever rule the different contribution of α and β in the sample D can be easily calculated by

$$y : (1 - y) = a : b$$

where y is the fraction of atoms in phase β and (1-y) is the fraction of atoms in phase α. In this scenario, since the “lever” has to be balanced, very little y has been formed while much more “(1-y)” remains and therefore the equation can be fulfilled [34].

4.2 Isothermal characterisation methods

In order to experimentally determine a phase diagram, various different analysis methods have to be utilized and evaluated in agreement with each other. Samples, quenched after being annealed, are probed using isothermal characterisation methods, such as X-ray powder diffraction, scanning electron microscopy and optical microscopy, and dynamic characterisation methods like DTA.

4.2.1 X-ray powder diffraction and Rietvield refinement method

X-ray powder diffraction is an excellent phase identification technique due to the easiness of sample preparation and the possibility of multi-phase analysis. X-rays are generated by heating a tungsten cathode at very high voltage and focusing emitted electrons on an anode. Anode materials, which are often used are Cu or Mo (rarely Cr, Fe or Ag). Each anode material provides a characteristic X-ray spectrum and continuum (white radiation). Since the white radiation is unwanted it must be eliminated by a monochromatic filter introduced in the pathway of the light. It usually consists of a material on atomic number lower than the anode material. The characteristic X-ray spectrum occurs because of electrons of higher orbitals dropping into lower energy orbitals; K_α radiation if the electron drops from a 2*p* orbital, K_β radiation if the origin orbital was 3*p*, which are both further divided into $K_{\alpha1}$, $K_{\alpha2}$ and $K_{\beta1}$, $K_{\beta2}$ respectively due to different spin states. The interfering K_β duplet is also eliminated with the introduced monochromatic filter.

In this way produced X-rays are diffracted by a periodic lattice, if the wavelength of the radiation has the same magnitude as the atomic distance planes (or layers) of the material according to Bragg’s law. The planes refer to

crystallographic planes described by the Miller indices (h/k/l). Each set of planes causes diffraction of the X-rays under a certain angle θ.

$$2 * d_{hkl} * \sin\theta = n * \lambda$$

There are two different methods established for powder diffraction analysis. On the one hand the powder diffractometer using the Bragg-Brentano pseudo focusing geometry, which may operate in reflection or transition mode. This method can be carried out with θ/θ or with θ/2θ geometry. θ/θ geometry means that the source and the detector are moving on the same circle under the same angle. θ/2θ geometry conditions are achieved when sample and detector are moving. While the sample is changes by the angle θ, the detector migrates by 2 θ. A modern detector for fast sample analysing is the Si-strip detector. It combines a high number of Si-strips, which allows to detect a certain angular range at once and yields the total signal by adding the different strips. If a material with high X-ray fluorescence is investigated an energy dispersive detector is needed (solid state detector). Strong X-ray fluorescence occurs for instance while measuring Fe with Cu-radiation.

The second method is the Guinier type camera, which is usually used in transmission mode. This method is advantageous by yielding high intensities due to the simultaneous detections of the whole diffractogram (angles range) and uses an image plate as detection method, which has a better noise to background ratio.

Evaluation of powder pattern is done by refinement of crystal structure information utilizing a least square fit of a theoretical pattern in comparison to the measured powder pattern. This technique is named Rietveld method. As indicated it is essential to have knowledge about the structure of all occurring phases. Consequential it is difficulties arise for X-ray powder diffraction to directly determinate crystal structure. This is usually done using single crystal X-ray diffraction if possible.

The most important part of the Rietveld refinement is the comparison of calculated (y_{Ci}) and observed intensities (y_{Oi}) of an obtained powder pattern utilizing a least square algorithm. A weight factor is introduced in each calculation (w_i) because of the background noise. The important factor for the refinement, in

accordance with the fitting of the calculated plot, is the weighted R-factor (R_{wP}), which is desired to be minimized.

$$x_i^2 = \frac{\sum_i w_i * (y_{Oi} - y_{Ci})^2}{\sum_i w_i * y_{Oi}}$$

$$R_{wP} = \sqrt{\frac{\sum_i w_i * |(y_{Oi} - y_{Ci})|^2}{\sum_i w_i * y_{Oi}}}$$

Nevertheless, a separate inspection of the refinement by hand is essential in order to get a profound evaluation of X-ray powder diffraction pattern. Besides quantitative and qualitative composition of the measured sample other important data can be acquired such as crystallographic information, crystallite size and preferred orientation can be gained from powder refinements [35-38].

4.2.2 Optical microscopy

Analysing the surface of an opaque metal or alloy, via optical microscopy under different examination modes with different magnifications, is the most straight forward method to obtain valuable information. This method enables access to physical and in seldom cases chemical properties of the constituents. Thermal history, the number of phases, the grain size, the crystallization sequence and the reaction types can be obtained. Sometimes even segregation, precipitation and twinning can be seen. To acquire valuable information a careful sample preparation is obligatory.

The most conventional starting point is the bright field imaging mode. A paralleled light beam is reflected on the surface of the sample and observed through an ocular (mono or binocular). Any sample roughness is easily observable because less light is reflected into the eyepiece and therefore appearing darker than smooth surfaces. Different phases can often be identified due to their different albedo on colour. Another information, which can be derived from bright field microscopy is the crystallization sequence of the sample.

The second method, the dark field imaging mode, changes the path of the light beam to hit the sample under a very low angle. Therefore, only light beams generated through being scattered on an edge contributes to the observed image.

This leads to an inverted picture in respect to the light field method. With this mode grain boundaries can be seen and, furthermore, all scratches, holes and rough parts are visible. This information can be used for polishing optimization.

An imaging mode to detect height differences is the differential interference contrast (DIC). The incoming beam is polarized and afterwards separated by a bi-refringent prism into two parts. Any height difference (Δh) would lead to a different optical path length of the light beam. The resulting beam interference is according to Δh. The prominent information gained is the hardness of the different constituents. The higher a surface appears the harder is the phase, since less material is removed during polishing steps. Also, this method can be used for phase identification if the light field imaging mode has a bad contrast.

The distinct phases in polycrystalline materials can be identified via a polarisation imaging mode. Additionally, grain structure and preferred orientation can be observed by using the polarization mode. The beforehand polarized beam is, consistent with the optical properties of the analysed material, modified and after passing through the analyser providing contrast. Different strong polarization ability can be identified by rotating the sample relative to the incoming beam, which yields information about the symmetry of the phases. Phases with low polarizability are mostly of higher symmetry, whereas high polarizability leads to the conclusion of lower symmetry [39-42].

4.2.3 Scanning electron microscopy and microprobe analysis

Scanning electron microscopy and microprobe analysis introduce various possibilities for material characterisation. Besides the optical applications for microstructure and topographical analysis, which are better than the optical microscopy due to the higher resolution, it is also possible to acquire qualitative and quantitative information about the composition of the material.

The construction of the electron gun needed to produce an extremely focused electron beam can be compared with the X-ray tubes. A high voltage (15-50kV) is induced between the cathode (LaB_6 tip or tungsten filament) and a ring anode. In order to reduce the angle under which the electrons are emitted, a Wehnelt cylinder is introduced. The spot size of the beam is further reduced by condenser lenses and can be altered to determine the magnification under which the sample can be seen. A high vacuum is crucial for the measurement since it prevents losses of the electron beam due to scattering.

Imaging the surface of the sample is accomplished through backscattered electrons and secondary electrons. After the beam electrons enter the specimen they encounter elastic and inelastic scattering. After many evens of elastic scattering, where the direction is altered by an angle greater than 90° backscattered electrons may leave the material. These high energy electrons are highly dependent on the atomic number of the specimen and therefore the contrast is primarily given by the average atomic number. Secondary electrons occur along the path of the incoming beam or backscattered electrons. Since secondary electrons only have low energies they are only able to leave the sample neat the surface and can be used for topographical inspection. Both generated electron species are detected via a scintillation counter. Also, other radiative or non-radiative mechanisms can provide diverse information such as fluorescence X-rays, characteristic X-rays, Auger electrons or phonon generation, which can all be detected by several spectroscopy methods.

For qualitative and quantitative analysis of single or multicomponent materials the electron microprobe analyser is the most important instrument. This

method utilizes characteristic wavelengths with unique energy, whereby the wavelength is related to the atomic number according to Mosley's law:

$$\lambda^{-1/2} = C * (Z - \sigma)$$

C and σ are constants, while λ is the wavelength and Z the atomic number.

As detection systems two different dispersive X-ray spectroscopy methods can be used, one being energy-dispersive (EDX) and the other being wavelength-dispersive (WDX). EDX is based on recording the whole spectrum at the same time with a solid-state detector (energy versus counts) with the advantage of measuring very fast for the cost of limited energy resolution. WDX on the other hand has a goniometer-based setup, where single wavelengths are counted with a scintillation counter. To detect different wavelengths the analysed specimen and the detector must move along a focusing circle. The advantage of the later method is the better resolution for high quality analysis and the ability to measure light elements, while having the disadvantage of being slower due to the moving parts.

To be able to perform quantitative analysis calibration with standard material is obligatory. For metallic samples all elements contained must be used as standards. The intensities of the characteristic lines are evaluated in order to realise quantitative analysis. These intensities (I) are corrected for each element depending on the atomic number (Z), the X-ray fluorescence (F) and the absorption (A), with the weight fraction (w) as result. The total weight percent of the corrected data is very important for the reliability of the measurement and has of course to be around 100% [40, 43, 44].

$$\frac{C_x}{C_{(x)}} = \frac{I_x}{I_{(x)}} = k_x$$

$$\frac{C_x}{C_{(x)}} = [ZAF]_x \frac{I_x}{I_{(x)}} = [ZAF]_x k_x$$

$C_{(x)}$, C_x…mass concentration x in standard or sample

$I_{(x)}$, I_x… characteristic line intensity x in standard or sample

k ("k-ratio")… first approximate of mass concentrations for the element x in standard or sample

4.3 Dynamic characterisation methods

4.3.1 Differential thermal analysis (DTA)

DTA is a measurement technique, where endothermic (heat requiring) and exothermic (heat providing) phase transitions can be monitored as a function of temperature.

The sample and a reference, both being in the same type of crucibles (for example Al_2O_3 or quartz glass), are positioned onto the sample holder. An important feature of the reference is not having a phase transition in the measured temperature range as it would alter the base line and therefore maybe distort the results. It is heated by a beforehand set temperature program until the sample is fully melted. Oxidation of the sample is avoided by using inert gas flow while running the measurement.

On the bottom of the crucibles two thermocouples are located, which are recording the temperature difference between the sample and the reference. This difference in temperature occurs because the sample is undergoing a phase transition, where heat is required or released, while the reference is heated at the same rate all the time.

The resulting diagram, where the temperature difference is plotted against the reference temperature, can be evaluated by the shape of the curves for different occurring effect types. Invariant effects, where $f = 0$, take place at a fixed temperature yielding a steep peak ideally being only at the exact temperature of the effect. Non-invariant effects, where $f > 0$, occur at a temperature range and can have multiple different shapes. Since the measurement is not done with a heating rate being infinitely small delayed heat transfer can be seen. This leads to invariant effect peaks being asymmetrical and not being exactly at the invariant temperature. Also supercooling often occurs, while cooling curves are monitored. This leads to a solidification temperature lower as it ideally would be [33, 41, 45].

5. Experimental

5.1 Sample preparation

Since the aim of this work is the basic understanding of the Sb-rich part of the Sb-Te system, the first sample group was prepared to yield a perspective of further investigations of the system. These are listed in table 5.1 as samples 1A to 1J The preparation methods were eventually altered according to new findings.

5.1.1 Sample variety

All samples were prepared as seen in table 5.1. The basic materials were weight out to a sample mass of 1 g, with a maximal deviation of ±0.5mg from the calculated mass for each element, using a semi-micro balance (Sartorius research, R200D).

The following high purity elements were used:

- Sb metal
- Te metal

Table 5.1: Compositions of all prepared samples. Nominal and real compositions shown. Samples marked with an [*] were prepared as bulk samples.

Sample	Nominal composition [at.%]		Real composition [at.%]		Total mass [mg]
	Sb	Te	Sb	Te	
1A*	86	14	86,03	13,97	1000
1B*	82	18	82,01	17,99	1000
1C*	78	22	77,99	22,01	1000
1D*	74	26	73,98	26,02	1000
1E*	70	30	70,01	29,99	1000
1F*	66	34	66,00	34,00	1000
1G*	62	38	61,99	38,01	1000
1H*	58	42	58,00	42,00	1000
1I*	54	46	54,01	45,99	1000
1J*	50	50	50,02	49,98	1000
1.5A	86	14	85,89	14,11	500
1.5B	82	18	81,96	18,04	500
1.5C	78	22	77,90	22,10	500
1.5G	62	38	62,00	38,00	500
1.5H	58	42	58,02	41,98	500
1.5I	54	46	53,98	46,02	500
1.5J	50	50	50,03	49,97	500
1.5 alpha	90	10	90,03	9,97	500
1.5 beta	94	6	94,01	5,99	500
DTA_Bulk_B*	82	18	81,70	18,30	100
2alpha	92	8	92,07	7,93	500
2A	88	12	87,93	12,07	500
2B	84	16	83,93	16,07	500
2C	80	20	80,00	20,00	500

Continuous on the next page

Table 5.1 continued from the previous page

Sample	Nominal composition [at.%]		Real composition [at.%]		Total mass [mg]
	Sb	Te	Sb	Te	
2D	76	24	76,02	23,98	500
2E	72	28	71,97	28,03	500
2F	68	32	67,93	32,07	500
2G	64	36	64,02	35,98	500
2H	60	40	60,06	39,94	500
2I	56	44	56,03	43,97	500
2J	52	48	52,01	47,99	500
2K	47	53	46,72	53,28	500
2L	40	60	40,07	59,93	500
2M	42	58	41,99	58,01	500
2N	45	55	45,02	54,98	500

5.1.2 Sample treatment

The usual sample treatment procedure would start with the melting of the sample in an arc furnace. However due to the high vapor pressure of Sb and Te, the weight loss would be too massive to be negligible, which made it impossible to use an arc furnace for melting the samples. Therefore, a less invasive method had to be used in this study. First evacuated quartz tubes, containing the sample, were prepared by applying vacuum (around 10^{-3} mbar) and flushing with Argon 3 times before sealing them using a H_2/O_2 flame.

The samples inside were gently melted using a H_2 flame and shaken to ensure proper mixing of the components. During the melting process arising gaseous Te, noticeable through a green gas phase, deposited on the cooler end of the quartz tube and had to be returned to the sample. It was heated until no excess material was observable on the quartz tube.

All samples after the first series (1.5alpha to 2N; see table 5.1) were powdered and pressed to pellets afterwards to get a better homogeneity in the sample. The pills, with a diameter of 5 mm, were pressed at approximately 25 kN for 1.5 minutes, with a hydraulic press (Larzep, EC10.13).

5.1.3 Equilibration

The bulk samples and powder pills were sealed into evacuated quartz tubes using a H_2/O_2 flame as described before. After examining leakproofness, all samples were annealed in a muffle furnace. Annealing length and temperature program can be seen in table 5.2. After the annealing length was reached the samples were quenched using water to freeze the thermodynamic conditions at the certain temperature.

Bulk samples and powder pills were carefully crushed into suitable pieces for the upcoming investigations. Examination method usage can be found in table 5.2. Bigger sample pieces could be used for DTA and embedding into resin for metallographic investigations. Small pieces and powder was used for XRD analysis.

Table 5.2: Temperature program, annealing time and evaluation method of all samples. Samples marked with an [*] were prepared as bulk samples.

Sample	Annealing time	Annealing Temperature [°C]	Characterization method			
			X-ray powder diff.	DTA	Optical Microscopy	SEM
1A*	2 weeks	520	√	√	√	√
1B*	2 weeks	520	√	√	√	√
1C*	2 weeks	520	√	√	√	√
1D*	2 weeks	520	√	√	√	√
1E*	2 weeks	520	√	√	√	√
1F*	2 weeks	520	√	√	√	√
1G*	2 weeks	520	√	√	√	√
1H*	2 weeks	520	√	√	√	√
1I*	2 weeks	520	√	√	√	√
1J*	2 weeks	520	√	√	√	√
1.5A	2 weeks	520	√	√	-	√
1.5B	2 weeks	520	√	√	-	√
1.5C	2 weeks	520	√	√	-	√
1.5G	2 weeks	520	√	√	-	√
1.5H	2 weeks	520	√	√	-	√
1.5I	2 weeks	520	√	√	-	√
1.5J	2 weeks	520	√	√	-	√
1.5 alpha	2 weeks	520	√	√	-	√
1.5 beta	2 weeks	520	√	√	-	√
DTA_Bulk_B*	-	-	-	√	-	-
2alpha	2 weeks	520	√	√	-	√
2A	2 weeks	520	√	√	-	√
2B	2 weeks	520	√	√	-	√
2C	2 weeks	520	√	√	-	√

Continues on the next page

Table 5.2 from previous page continued

Sample	Annealing time	Annealing Temperature [°C]	Characterization method			
			X-ray powder diff.	DTA	Optical Microscopy	SEM
2D	2 weeks	520	√	√	-	√
2E	2 weeks	520	√	√	-	√
2G	2 weeks	520	√	√	-	√
2H	2 weeks	520	√	√	-	√
2I	2 weeks	520	√	√	-	√
2J	2 weeks	520	√	√	-	√
2K	2 weeks	520	√	√	-	√
2L	2 weeks	520	√	√	-	√
2M	2 weeks	520	√	√	-	√
2N	2 weeks	520	√	√	-	√

5.1.4 Embedding

Samples usable for embedding should have one side being relatively flat to reduce the grinding time especially for powder sample, which are especially fragile. The samples were embedded in conducting, phenolic, hot mounting resin with carbon filler (PolyFast, Struers). Therefore, at a pressure of 15 kN, the resin was heated to 180°C for 6 minutes and cooled with water for an additional 3 minutes at the same pressure (used: LaboPress-1, Struers). To smoothen the surface, the resin block is added into a polishing machine (used: LaboPool-6, Struers), abrasive SiC paper is used. For polishing purposes 1 µm and 0.3 µm grain size Al_2O_3 powder (Micropolish II, Buehler) was used.

5.1.4 Sample preparation difficulties

Since both elements, which are used in this thesis, have a very high vapor pressure, standard preparation methods, like melting via an arc furnace could not be utilized. Therefore, the preparation method had to be altered as discussed in chapter 5.1.2. While preparing the evacuated quartz glass loaded with the samples, it was necessary to avoid Te loss due to unwanted heating of the metal mixture. This has to be considered especially when preparing DTA samples, which are short in length.

Another difficulty worth mentioning is the preparation for the measurements. Both bulk and pressed powder samples had to be crushed with a WC mortar to obtain small pieces, which is easy for the bulk samples. However, the pressed powder samples had to be prepared with caution to obtain sample pieces large enough to be able to perform DTA measurements and embedment. Also, while polishing powder samples it had to be ensured to neither use to much clamping pressure nor to grind the samples for too long, since the surface of the sample would chip away completely. Furthermore, the polishing state of the powdered samples could not be verified using the dark field mode of the optical microscope, due to porous character of the pressed pills.

5.2 Measurements

5.2.1 X-ray powder diffraction

For structure refinement and phase identification X-ray powder diffraction was used. The samples were powdered with a WC mortar and fixed on a Si single crystal sample holder using grease. The sample was attached to the auto sampler of the powder diffractometer (D8, ADVANCE, Bruker) using a Bragg-Brentano pseudo focusing goniometer with θ/2θ geometry. Detector for all measurements was a silicon strip detector (Lynxeye). Since the samples did not contain elements generating X-ray fluorescence, measurements with an energy dispersive detector (SolX) were not needed. Ni was used as K_β – filter.

All samples were measured for 1 hour with an acceleration voltage of 40 kV and a current of 40 mA. Rietvield refinements, phase and structure evaluations were done using the Topas software (Topas 4, Bruker). For further investigations on Incommensurate modulated phases the software Jana was used (JANA2006) [46].

5.2.2 Differential thermal analysis (DTA)

To investigate phase transitions and their corresponding temperatures DTA was used (DSC 404 F1 Pegasus®, Netzsch). Samples of approximately 100 mg were prepared in evacuated quartz tubes as described in chapter 5.1.2, then placed onto the sample holder. As reference material 100 mg Zr, which has no phase transition in the applied temperature range, was placed also in an evacuated quartz tube.

The samples were heated in two cycles above the anticipated melting point with a heating rate of 5 K per minute (see table 5.3 and figure 5.1).

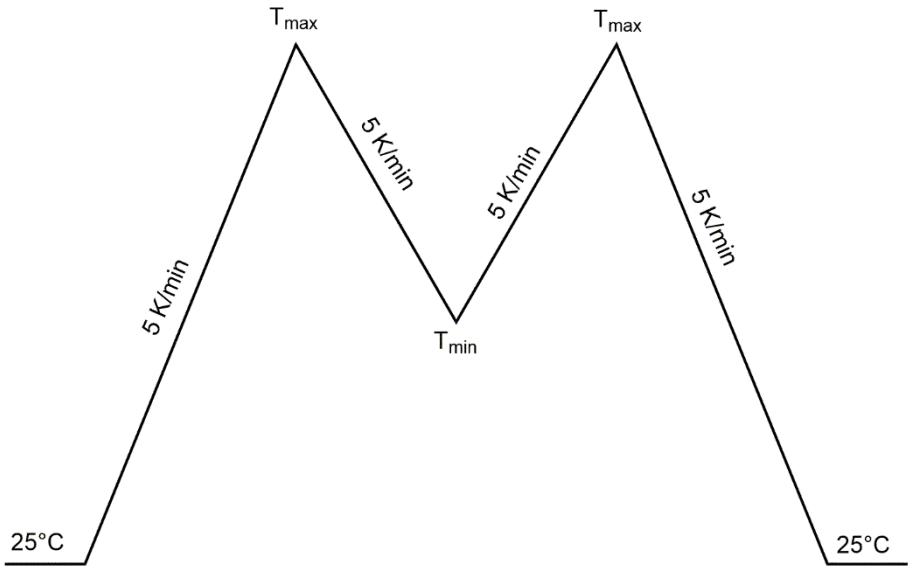

Figure 5.1: General temperature profile used in all DTA measurements.

Sample	T_{max} [°C]	T_{min} [°C]	Sample	T_{max} [°]	T_{min} [°C]
1A	640	500	1.5 α	670	500
1B	640	500	1.5 β	670	500
1C	640	500	2 α	670	500
1D	600	500	2A	640	500
1E	600	500	2B	640	500
1F	600	500	2C	640	500
1G	600	500	2D	600	500
1H	640	500	2E	600	500
1I	640	500	2F	600	500
1J	640	500	2G	600	500
1.5A	640	500	2H	600	500
1.5B	640	500	2I	640	500
1.5C	640	500	2J	640	500
1.5G	640	500	2K	640	500
1.5H	640	500	2L	640	500
1.5I	640	500	2M	640	500
1.5J	640	500	2N	640	500

Table 5.3: Maximum and minimum temperature used for DTA measurements.

Even though the samples were sealed in evacuated quartz glass tubes, 3 evacuation/refill purging steps were carried out before each measurement and a constant Ar-flow was ensured.

Calibration of the DTA apparatus was done by acquire the melting temperature of the pure elements Sn, Zn, Te, Sb, Ag and Au. Temperatures were

measured with a Pt/Pt10%Rh thermocouple. Evaluations were done utilizing the Proteus® software (Netzsch).

5.2.3 Optical microscopy

The optical microscopy measurements were performed on a binocular reflected light microscope (Axiotech 100, Zeiss). Pictures of bright field, dark field, polarisation images and difference interference contrast images were taken. Only bulk samples were measured with this technique since the pressed powder samples did not yield meaningful results.

5.2.4 Scanning electron microscopy (SEM) and microprobe analysis (EPMA)

For quantitative evaluations of the embedded samples, a scanning electron microscope was used (Supra 55 VP, Zeiss) with an acceleration voltage of 20kV. Surface imaging was obtained with a secondary electron detector and a back scattered electron detector. For the microprobe analysis an energy dispersive detector (EDX) detector was used, which was calibrated with Co. The characteristic X-ray lines were calibrated with embedded pure elements of Te and Sb. Because of atomic number difference of 1 between Te and Sb, the mass contrast of the samples was very bad. Better observable was most of the time the orientation contrast, especially for the bulk samples [47].

6. Results and discussion

In the following all samples, lattice parameter obtained through XRD, DTA results, SEM/EPMA outcomes and refinement with the JANA software can be found chronologically, as tables, in the specific subsections.

A general overview is provided in the first batch of samples followed by in depth analysis with a different sample preparation process. The chapter is finalized with the JANA refinement and a phase diagram suggestion based on the results obtained through the various analysis methods.

6.1 First approach: bulk samples

All data gained about the first series of samples is showcased in table 6.1 and 6.2. Table 6.1 contains data from XRD and SEM/EPMA, whereas table 6.2 shows the differential thermal analysis outcomings.

Sample [at.% Sb/Te]	Phase	a [Å]	c [Å]	Average composition of all measured points [at.%]		Standard deviation [at.%]
				Sb	Te	
1A [86/14]*	-	-	-	86.23	13.77	1.91
1B [82/18]*	-	-	-	78.55	21.45	5.29
1C [78/22]**	-	-	-	77.60	22.40	2.09
1D [74/26]	Sb_8Te_3	4.280	64.220	74.56	25.44	0.88
1E [70/30]	Sb_2Te	4.277	17.612	70.23	29.78	0.32
1F [66/34]**	-	-	-	66.70	33.30	1.37
1G [62/38]**	-	-	-	61.85	38.15	5.77
1H [58/42]*	-	-	-	62.52	37.48	6.04
1I [54/46]**	-	-	-	53.53	46.47	3.84
1J [50/50]*	-	-	-	50.13	49.87	3.19

Table 6.1: Mean composition plus deviation aquired by electron microprobe analysis as well as lattice parameter and phases determined by powder X-ray diffractometry. [*] indicates that a phase could be refined but will be discussed at the related powder sample in chapter 6.2. [**] indicates no refineable phase for this sample.

Sample [at.% Sb/Te]	Solidus [°C]	Invariant [°C]	Liquidus [°C]
1A [86/14]	523.1	537.4	572.5
1B [82/18]	526.2	533.4	557.0
1C [78/22]	-	523.0	538.1
1D [74/26]	-	536.9	-
1E [70/30]	-	534.9	-
1F [66/34]	-	540.2	-
1G [62/38]*	-	535.7	596.0
1H [58/42]	-	538.1	569.9
1I [54/46]	-	536.6	581.5
1J [50/50]	-	538.2	596.4

Table 6.2: Differential thermal analysis data of the first sample series.

Sample 1G marked with [*] in table 6.2 has a liquidus temperature, which is not fitting into the picture of the other samples around. The sample was inhomogeneous (Te-rich), which lead to the circumstance that the piece used for DTA is not representative and therefore yielded a wrong result for the liquidus temperature. If the DTA results are compared to the work of Ghosh et al. [12] all measured temperatures are around 10 °C lower than in said work, which could occur be due to the inhomogeneity of the samples.

As elaborated in chapter 5, only the first batch of samples were prepared as bulk samples. The reason why the preparation method was changed is shown in table 6.1. As shown in table 6.1 the EPMA measurements yield a very big deviation

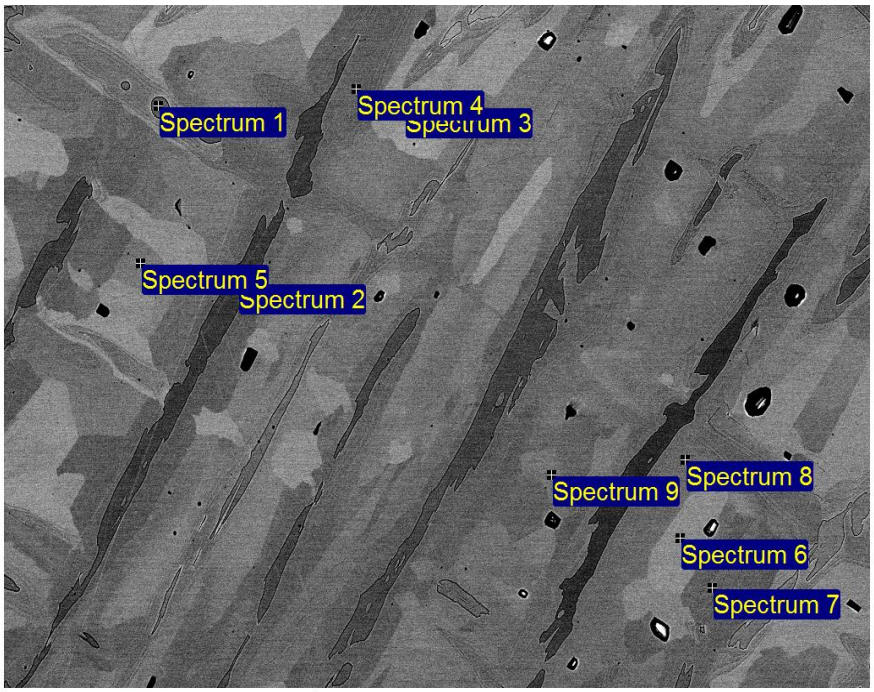

Figure 6.1: SEM picture of sample 1B.

for most of the samples except 1D-1F. This indicates that samples having a high deviation were not prepared homogeneous. In SEM examination grains with vastly different compositions were observable, however these distinct compositions could not be derived by the brightness of the grain. Figure 6.1 shows a SEM picture of sample 1B. Despite having the same composition of 77.5 at.% Sb, spectrum 6 and 8 have a very different brightness. This phenomenon occurs due to orientation contrast. Normal mass contrast is not reliably because of the similarity of atomic number of antimony and tellurium.

Spectrum 1 of figure 6.1 measures a grain of pure antimony surrounded by Sb-Te compounds. Further examination reveals segregation zones around such Sb areas, which can be seen in figure 6.2.

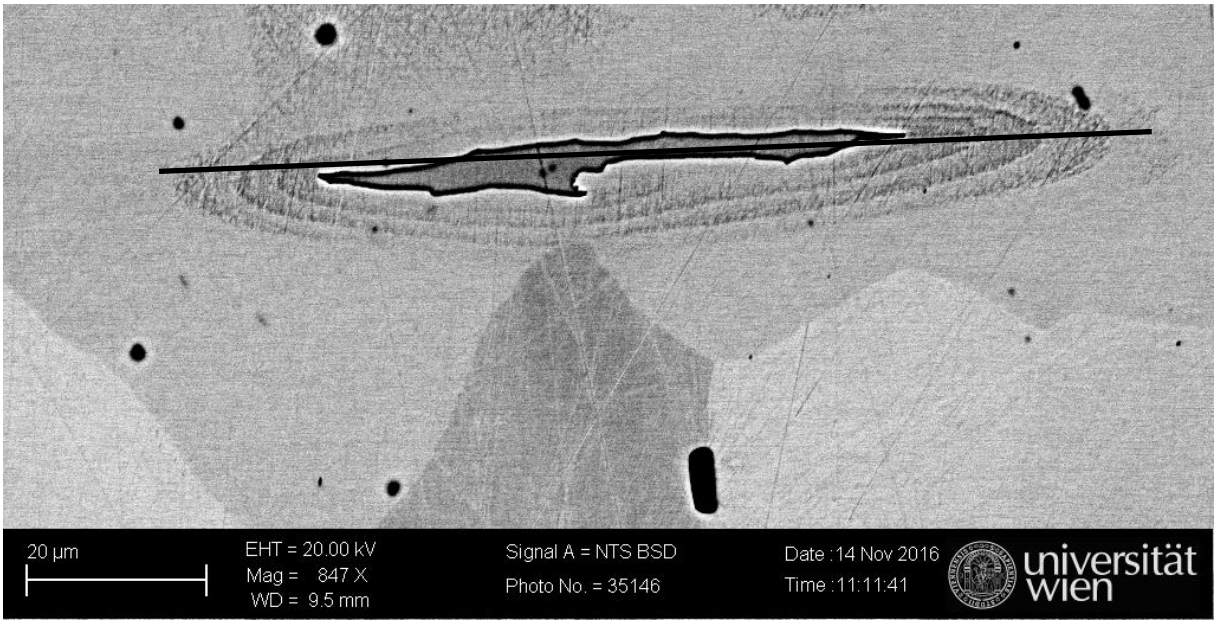

Figure 6.2: Segregation zone of sample 1C. The black line indicates the direction of the performed line scan.

This segregation was evaluated by performing line scans. Each circle has a different composition, with this highest Sb concentration being next to the pure Sb and a steadily decrease into the bulk. Figure 6.5 shows the result of the line scan of the above figure.

The same pattern can be found in the bulk samples 1B and 1A. Figures 6.3 and 6.4 are showing the examined segregation areas in these samples. The results are given in figures 6.5 to 6.7.

Figure 6.4: Segregation zone of sample B The black line indicates the direction of the performed line scan.

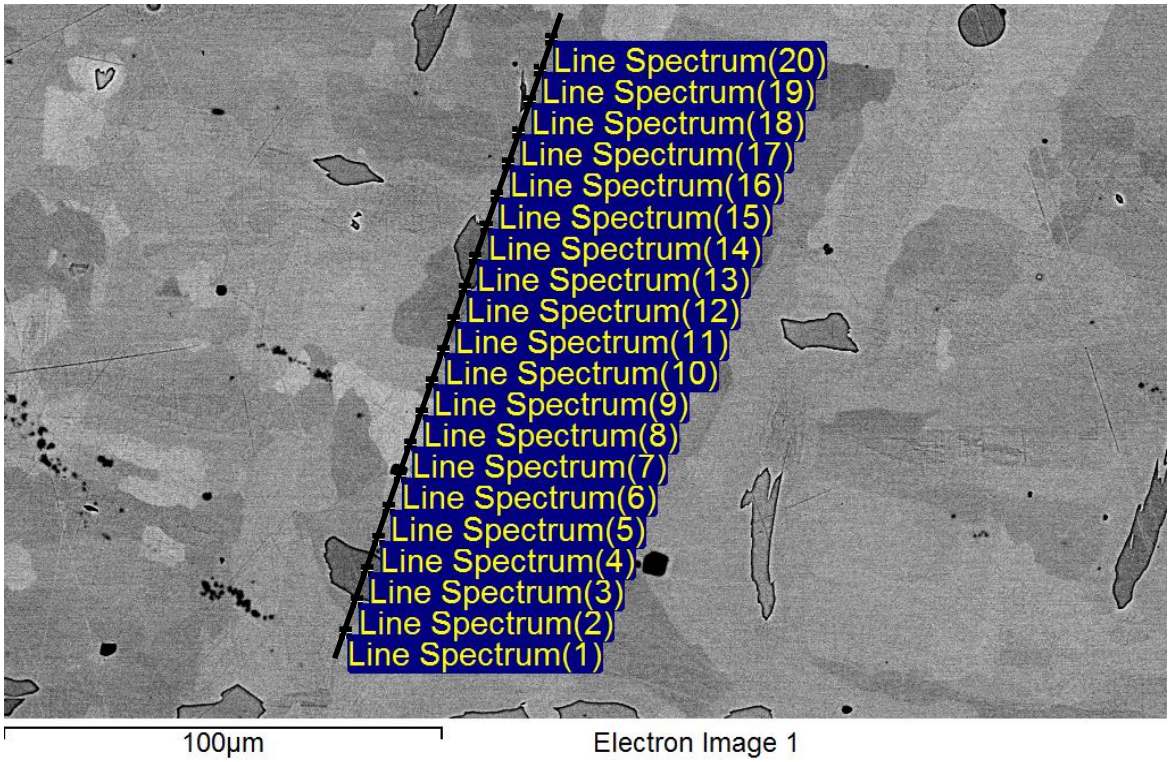

Figure 6.3: Segregation zone of sample 1A. The black line indicates the direction of the performed line scan.

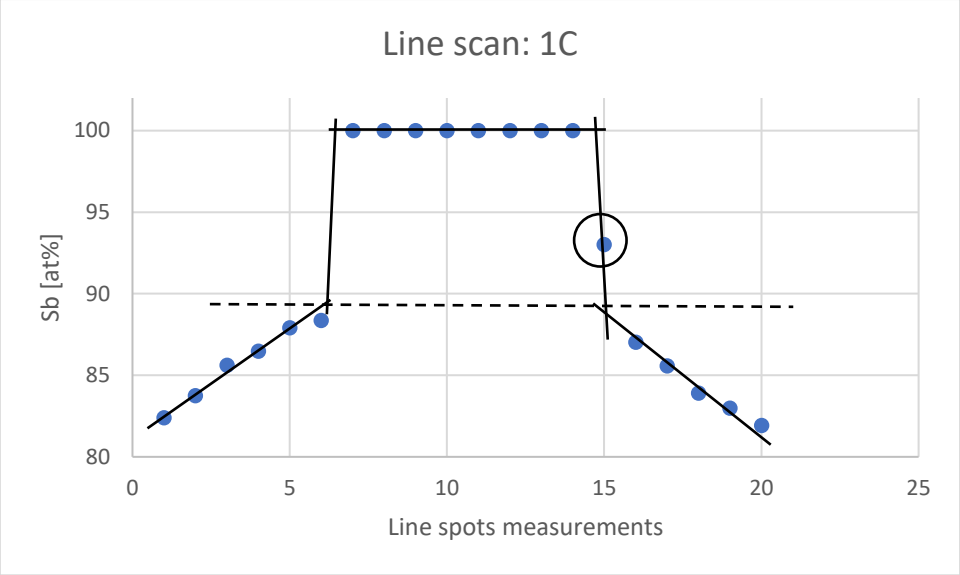

Figure 6.5: Line scan results of sample 1C. The circled measurement is assumed to be exactly at the grain boundary of Sb and the segregation area and therefore not included in further phase boundary assumptions.

All these three samples are inhomogeneous, which can be seen by the continuous variation of composition in different zones of the metal compound. If the final equilibrium state had been reached all Sb would be consumed, leaving a

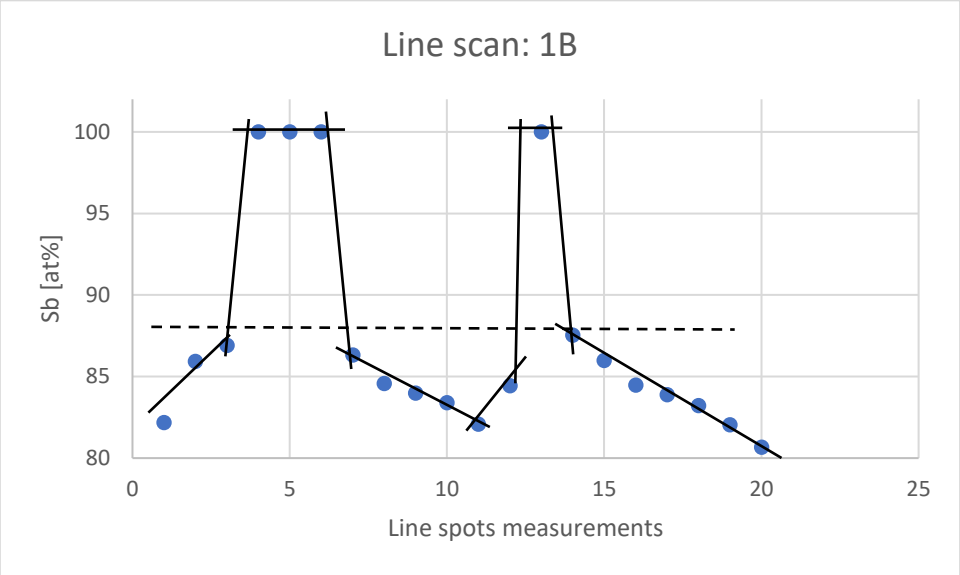

Figure 6.6: Line scan results of sample 1B.

single phase.

Regardless of the inhomogeneous behaviour, we can obtain valuable information, while looking at the grain boundaries between Sb and the segregation area. This would lead to the conclusion that the two-phase field between Sb and δ would range from pure Sb to 12 at.% Te, which is very different from the suggestion of the work of Ghosh et al [12].

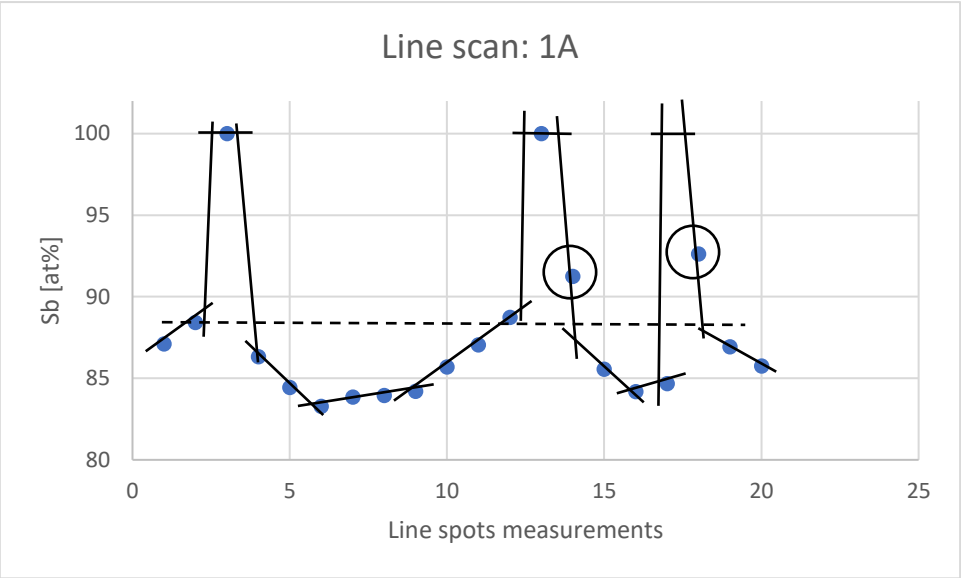

Figure 6.7: Line scan results of sample 1A. The circled measurement is assumed to be exactly at the grain boundary of Sb and the segregation area and therefore not included in further phase boundary assumptions.

As shown in table 6.1 sample 1D, 1E and 1F appeared to be homogeneous due to their small standard deviation of the average composition of the measured points. For sample 1D and 1E it was possible to be evaluated via Rietveld refinement using existing structures [11, 23].

Both refined structures can be derived from the Sb structure (As structure), with both having a trigonal unit cell. Both structures and all further, which will be discussed are built upon the subgroups shown in figure 6.8.

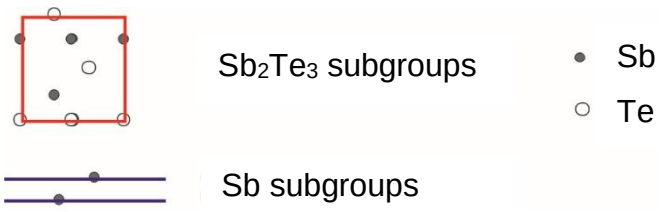

Figure 6.8: Subgroups, which are constructing the structures refined in this work.

In figure 6.9 the unit cells of the sample 1D (Sb_8Te_3) and 1E (Sb_2Te) can be seen. The first one having the space group 166 (R-3m) and the later one 156 (P-3m1). While comparing the composition noted in table 6.1 and the composition of the used superstructure, a discrepancy can be found leading to a tellurium depletion in this two samples. For instance, sample 1E should have 33.3 at% Te according to the structure but only has an average of 29.78 at.% Te, which was measured via EDX. A possible explanation could be a loss of Te due to its high vapor pressure.

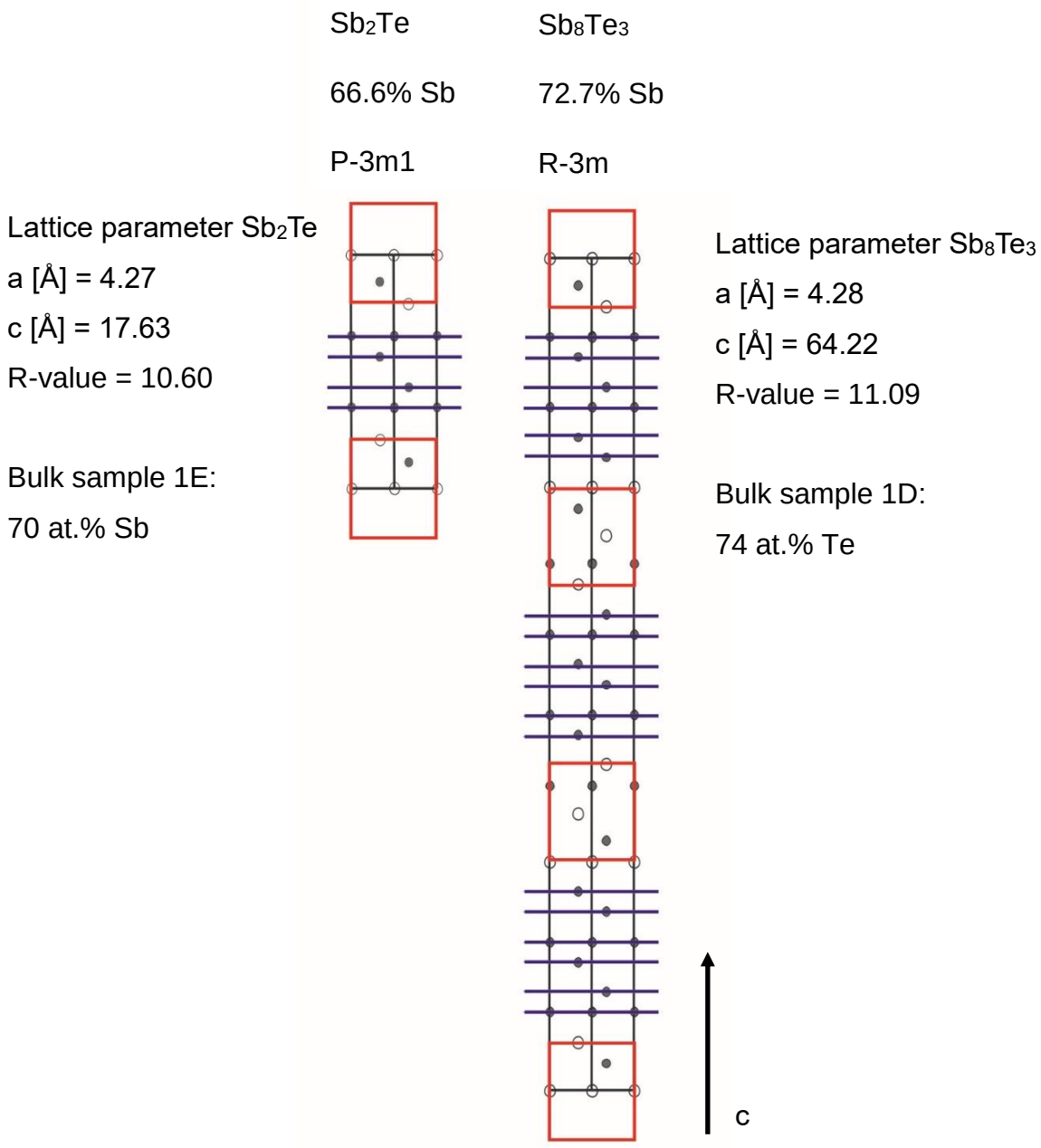

Figure 6.9: Unit cell of the samples 1E on the left and 1D on the right [11, 23].

Figure 6.10 and 6.11 show the Rietveld refined X-ray powder diffraction plots. They show that both structure models are perfectly compatible for those samples. Aside from a few intensity differences, all prominent and satellite reflections are fitted ideally with this model, which is crucial for a full interpretation.

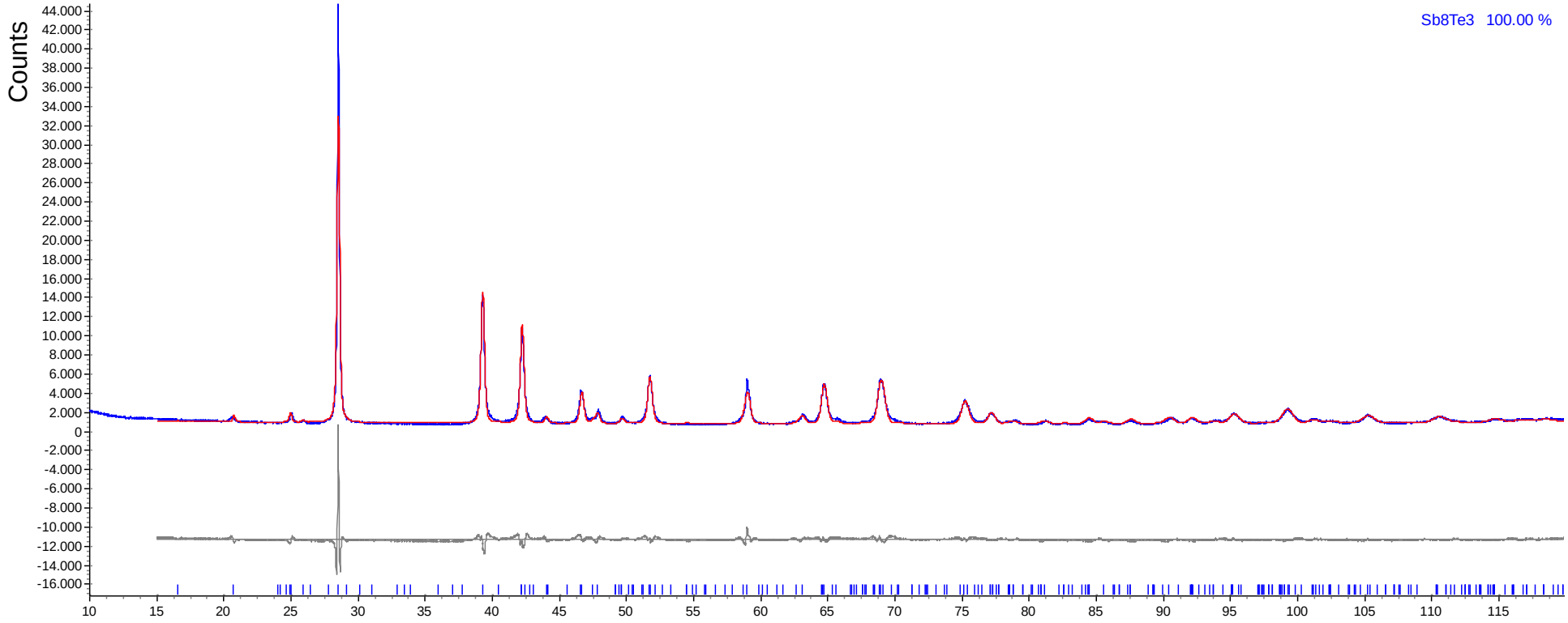

Figure 6.10: Calculated powder pattern of sample 1D using Rietveld refinement with the structure model of Kifune et al. [11].

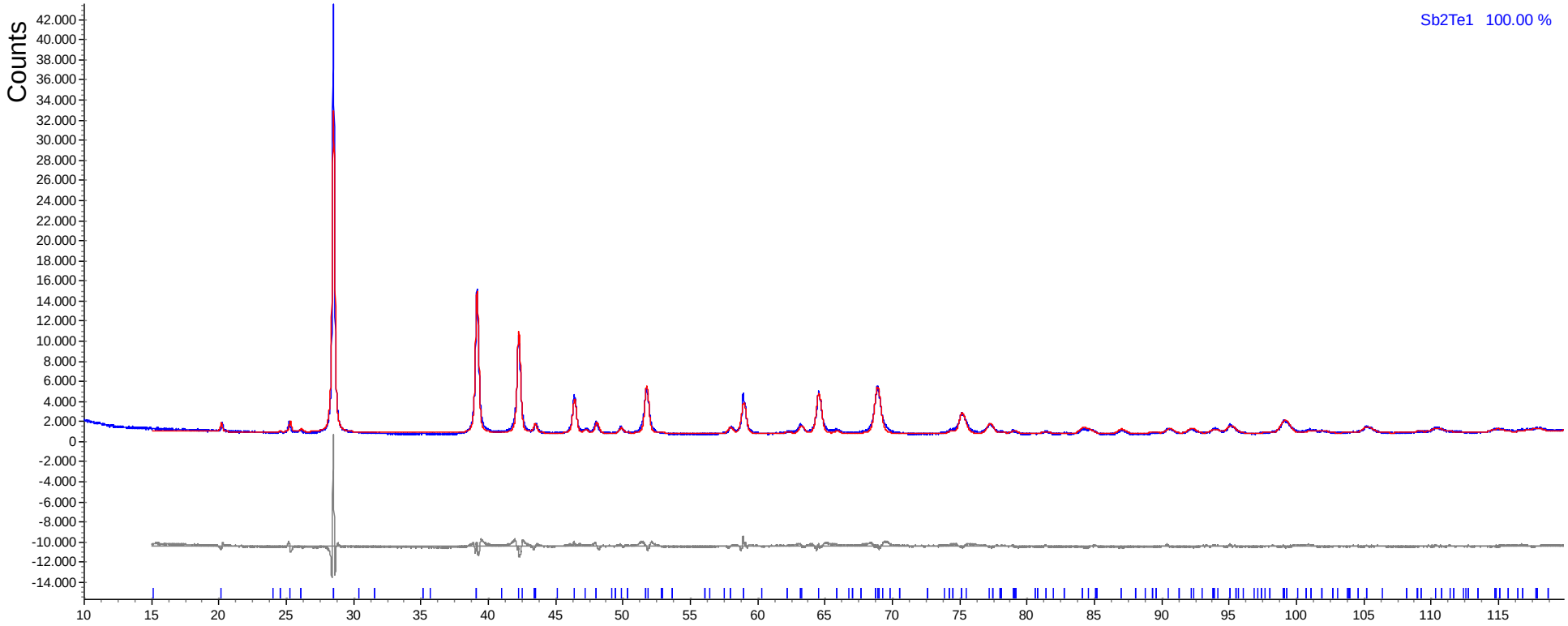

Figure 6.11: Calculated powder pattern of sample 1E using Rietveld refinement with the structure model of Shelimova et al. [23].

The main problem of the first bulk sample series is their inhomogeneity, which needed to be solved in order to get reliable data from all analysis methods. After noticing that the temperatures obtained from the DTA differ in the same direction for most of the samples, an idea of tempering while performing a DTA measurements emerged. Since the temperature difference of the inhomogeneous samples compared to literature is around 10 °C the concept was to heat slowly until the melting process starts, and then hold the temperature constant. The anticipated process was that the sample then starts homogenising while tempering. A following DTA measurement could then confirm the changed reaction temperature.

Therefore, the sample DTA_Bulk_B (see table 5.1) was prepared. Unfortunately, no phase transformation occurred at the anticipated temperature. The sample was nonetheless tempered for 6h at 528°C. A following SEM/EPMA measurement confirmed that the sample was still inhomogeneous, with and average composition of all measured spots of 18.39 at.% Te and a standard deviation of 4.96 at.%, compared to table 6.1 (bulk samples normally prepared) and 6.4 (powder samples). This heat treatment was consequentially dropped.

6.2 Pressed powder samples

After a few attempts to consistently gain homogeneous bulk samples, the preparation method was revised and focused around pressed powder samples.

All collected data relating to the pressed powder samples is shown in the tables 6.3 and 6.4, where table 6.3 contains data acquired through DTA and table 6.4 consists of XRD and SEM/EPMA results.

Sample [at.% Sb/Te]	Solidus [°C]	Invariant [°C]	Liquidus [°C]
1β_p [94/6]	-	547.5	614.5
2α_p [92/8]	-	547.2	607.5
1α_p [90/10]	-	547.4	598.9
2A_p [88/12]	-	546.9	591.7
1A_p [86/14]	-	546.5	582
2B_p [84/16]	542.7	546.8	578.5
1B_p [82/18]	-	545.8	569
2C_p [80/20]	541.5	547.8	563.8
1C_p [78/22]	538.7	548.7	554.2
2D_p [76/24]	538	544.6	-
2E_p [72/28]	-	539.3	-
2F_p [68/32]	-	540.2	-
2G_p [64/36]	-	541.2	-
1G_p [62/38]	-	540.2	-
2H_p [60/40]	540.2	545.2	558.6
1H_p [58/42]	539.5	548	567.8
2I_p [56/44]	539.7	551	575.1
1I_p [54/46]	539.5	552	584.2
2J_p [52/48]	539.5	550	591.1
1J_p [50/50]	539.4	552.5	598
2K_p [47/53]	538	554.1	607
2M_p [42/58]	540	552	610
2L_p [40/60]	-	612	-

Table 6.3: Acquired differential thermal analysis data of all powder samples.

Table 6.4: Data obtained from XRD and SEM/EPMA. Samples marked with [*] are found to be two phase samples and therefore having two mean compositions and deviations. [**] indicates no refinable phase for this sample.

Sample [at.% Sb/Te]	Phase	a [Å]	c [Å]	Average composition of all points [at.%] Sb	Te	Standard deviation [at.%] Sb	Te
1β_p [94/6]*				100	0	0.00	
	-	-	-	88.25	11.75	0.22	
2α_p [92/8]*				100	0	0.00	
	-	-	-	88.80	11.20	0.21	
1α_p [90/10]*				100	0	0.00	
	-	-	-	88.76	11.24	0.43	
2A_p [88/12]**	-	-	-	87.87	12.13	0.28	
1A_p [86/14]	$Sb_{48}Te_9$	4.293	109.107	85.96	14.06	0.38	
2B_p [84/16]**	-	-	-	83.30	16.70	0.43	
1B_p [82/18]	Sb_4Te	4.289	28.876	81.87	18.13	0.39	
2C_p [80/20]**	-	-	-	79.54	20.46	0.21	
1C_p [78/22]**	-	-	-	78.10	21.90	0.35	
2D_p [76/24]**	-	-	-	75.94	24.06	0.15	
2E_p [72/28]**	-	-	-	71.74	28.26	0.22	

Continues on next page

Table 6.4 continued from the previous page

2F_p [68/32]**	-	-	-	67.79	32.21	0.23
2G_p [64/36]**	-	-	-	64.27	25.73	0.17
1G_p [62/38]**	-	-	-	62.54	37.46	1.17
2H_p [60/40]**	-	-	-	59.37	40.63	0.44
1H_p [58/42]	Sb_4Te_3	4.272	83.309	57.91	42.09	0.76
2I_p [56/44]**	-	-	-	55.88	44.12	0.33
1I_p [54/46]**	-	-	-	53.72	46.28	1.17
2J_p [52/48]**	-	-	-	51.49	48.51	0.29
1J_p [50/50]	SbTe	4.269	24.050	50.46	49.54	1.34
2K_p [47/53]**	-	-	-	46.6	53.4	0.82
2M_p [42/58]*	-	-	-	40.84 43.14	59.16 56.86	0.22 1.16
2L_p [40/60]	Sb_2Te_3	4.263	30.467	39.55	60.45	0.17

Taking a closer look at table 6.4 it is shown that the obtained samples can be referred to as homogeneous, due to their small standard deviation of the average composition of all measured points. In addition, 4 samples were measured to contain 2 phases via SEM/EPMA, being the samples with high antimony content (1β_p, 1α_p and 2α_p) and the sample 2M_p.

The measured phase boundaries for the high antimony samples is on the one side pure Sb and on the other side around 11.5 at.% Te. This outcoming stands contrary to the work by Ghosh et al. [12] which claims the two phase field from pure Sb to 16.4 at.% Te. On the other hand, the obtained data verifies existing literature Brown and Lewis [26], Hanson and Anderko [27] and Kim and Chao [28] and is well in line with the analysis of the (inhomogeneous) bulk samples of the first sample series.

Through XRD evaluation of the powder samples another 4 structures could be refined, being $Sb_{48}Te_9$, Sb_4Te, Sb_4Te_3 and SbTe. These structures are also based on the two building blocks, Sb_2 and Sb_2Te_3, which are shown in figure 6.6. $Sb_{48}Te_9$ (powder sample 1A_p) and Sb_4Te (powder sample 1B_p) show the same behaviour as the structures, which were already found through the bulk samples, namely a discrepancy between the real composition (measured via EDX) and the composition given by the structure (see table 6.4 in comparison). The refined powder samples a lower concentration of Te than they should have. The powder samples Sb_4Te_3 (powder sample 1H_p) and SbTe (powder sample 1J_p) also displays this manner but with less extent. Figures 6.12 to 6.15 are showing the unit cells of the refined structures, whereas figure 6.16 to 6.19 contain the refined powder pattern. Besides a few intensities issues the structure models fit perfectly to the corresponding powder pattern. All 6 evaluated structures are superstructures of a trigonal unit cell, with an elongated c-axis.

In addition, a powder sample with the composition suitable to the structure Sb_2Te_3 was prepared and refined through the Rietveld method. The evaluated powder pattern is shown in figure 6.20. and serves as an ending point of the composition range of the structure evaluation.

$Sb_{48}Te_9$

84.2% Sb

R-3m

Lattice parameter $Sb_{48}Te_9$

a [Å] = 4.29

c [Å] = 109.11

R-value = 10.21

Powder sample 1A_p

86 at.% Sb

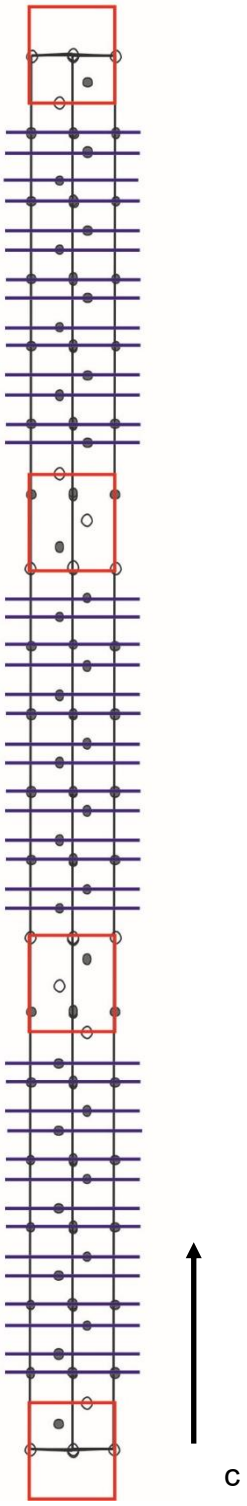

Figure 6.12: Unit cell of the superstructure $Sb_{48}Te_9$. As a basis, literature of Kifune et al. was used [11].

Sb_4Te

80% Sb

(hypoth.)

P-3

Lattice parameter Sb_4Te

a [Å] = 4.286

c [Å] = 28.86

R-value = 11.81

Powder sample 1B_p

82 at.% Sb

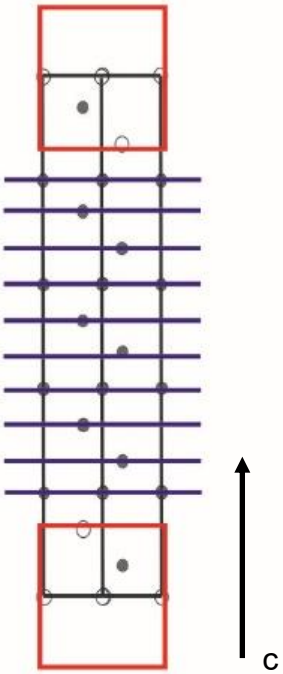

Figure 6.13: Unit cell of the superstructure Sb_4Te. As a basis, literature of Kifune et al. was used [29].

Sb_4Te_3

57% Sb

R-3m

Lattice parameter Sb_4Te_3

a [Å] = 4.27

c [Å] = 83.31

R-value = 9.87

Powder sample 1H_p

58 at.% Sb

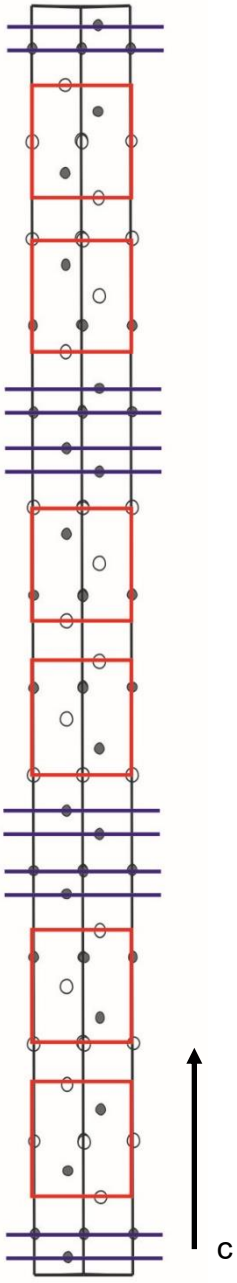

Figure 6.14: Unit cell of the superstructure Sb_4Te_3. As a basis, literature of Poudeu et al. was used [48].

SbTe

50% Sb

P-3m1

Lattice parameter SbTe

a [Å] = 4.269

c [Å] = 24.05

R-value = 10.21

Powder sample 1J_p

50 at.% Sb

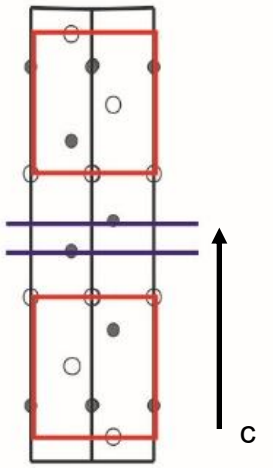

Figure 6.15: Unit cell of the superstructure SbTe. As a basis, literature of Stasova et al. was used [20].

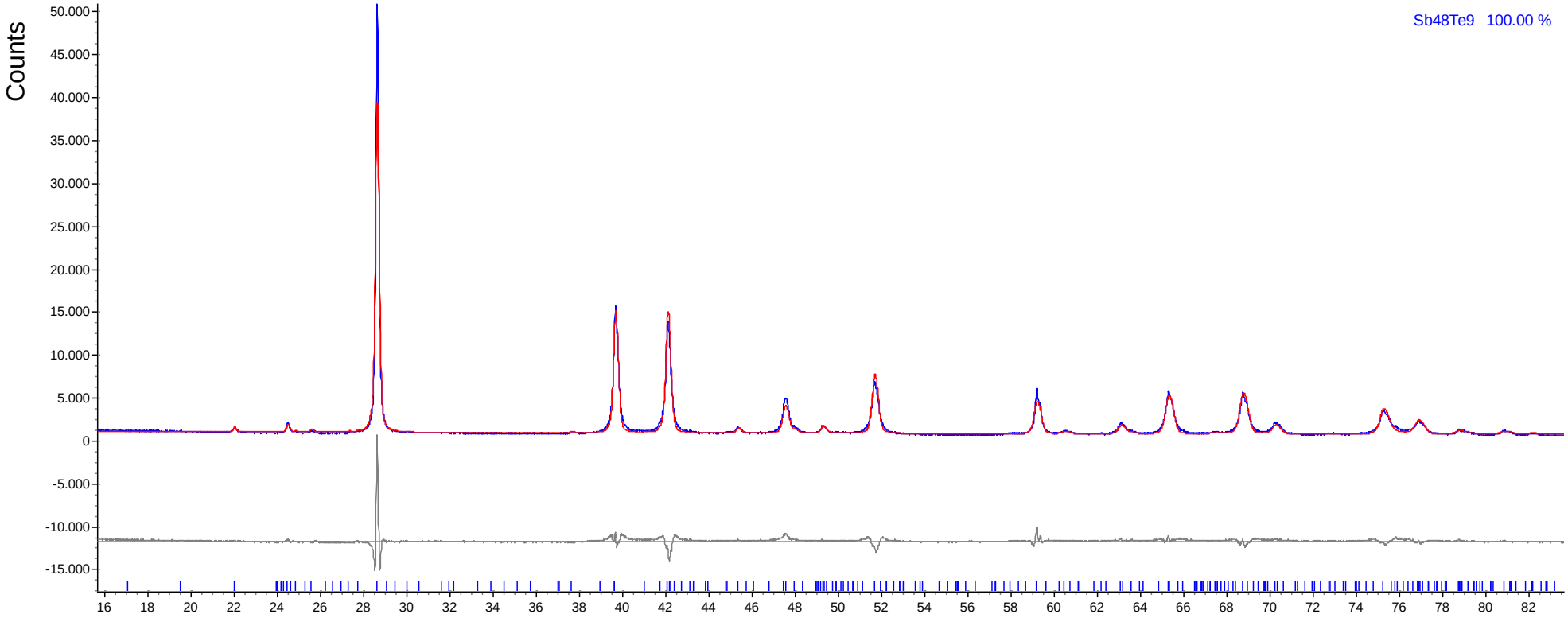

Figure 6.16: Calculated powder pattern of sample 1A_p using Rietveld refinement with the structure model of Kifune et al [11].

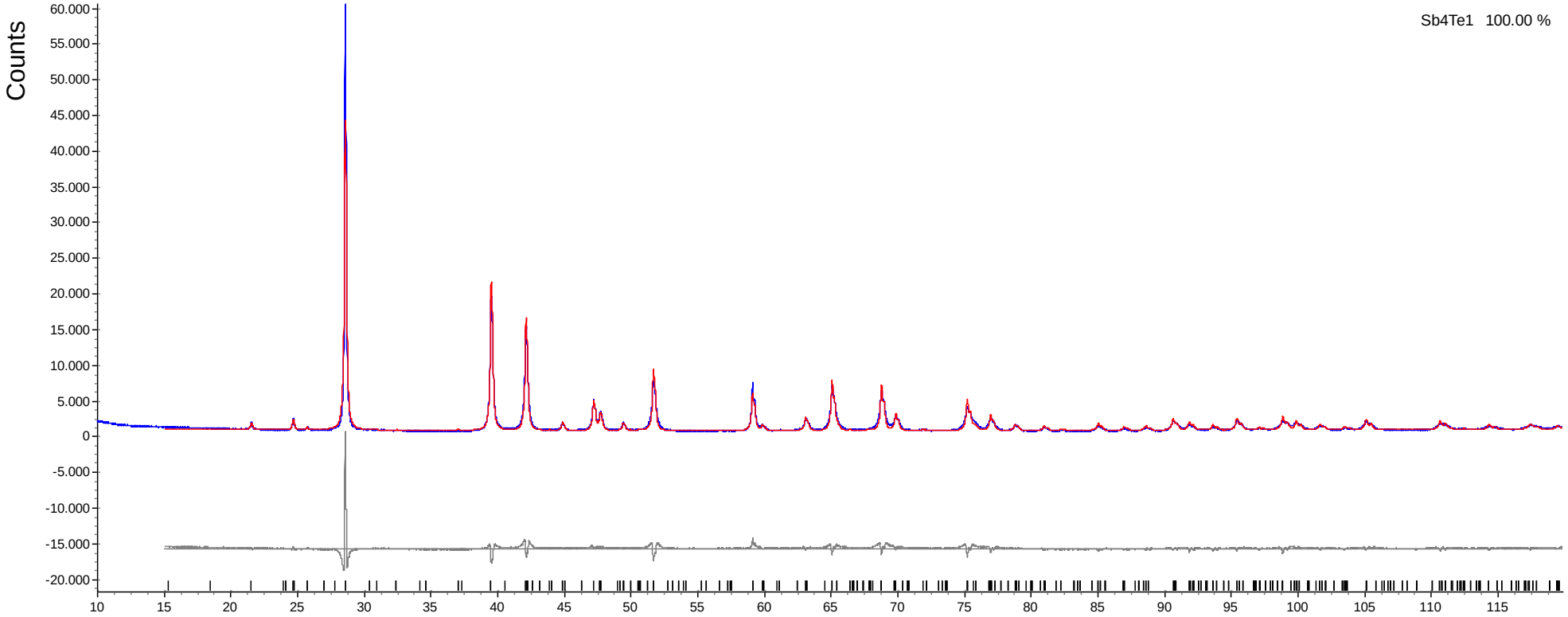

Figure 6.17: Calculated powder pattern of sample 1B_p using Rietveld refinement with the structural model of Kifune et al. [29].

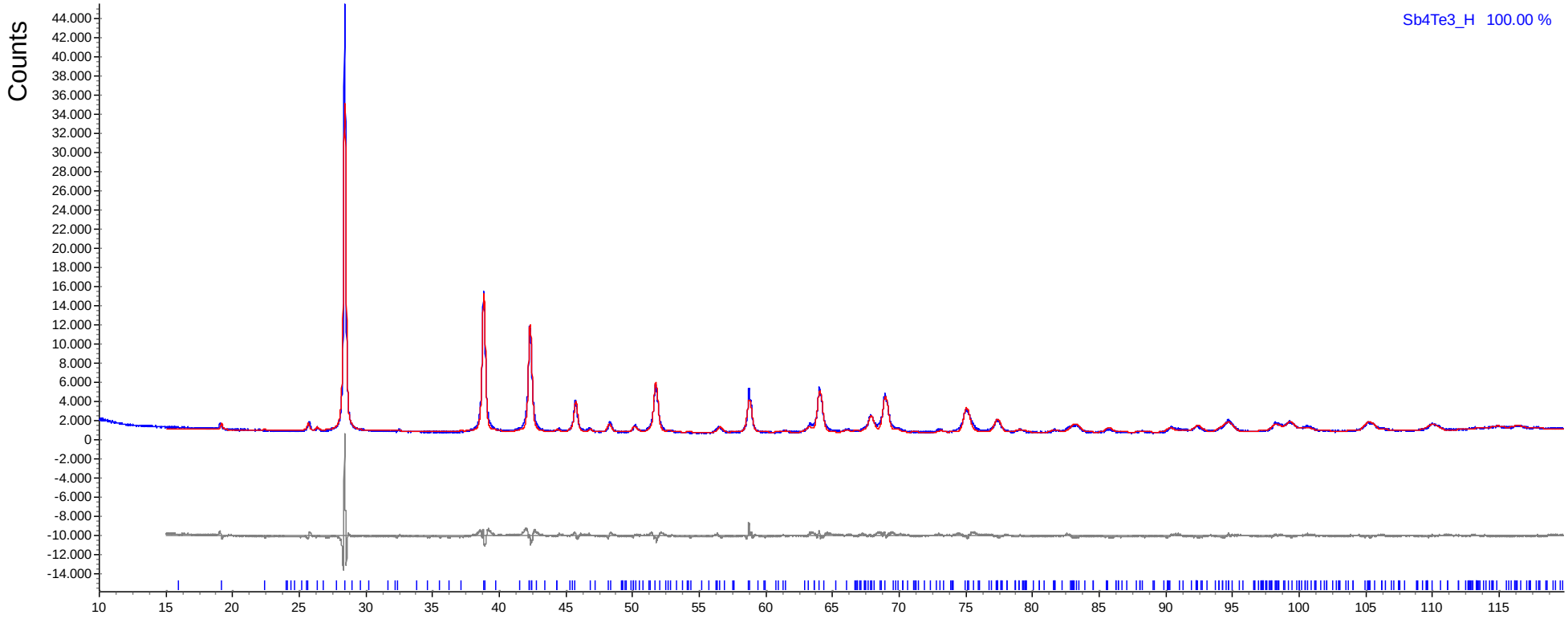

Figure 6.18: Calculated powder pattern of sample 1H_p using Rietveld refinement with the structure model of Poudeu et al [48].

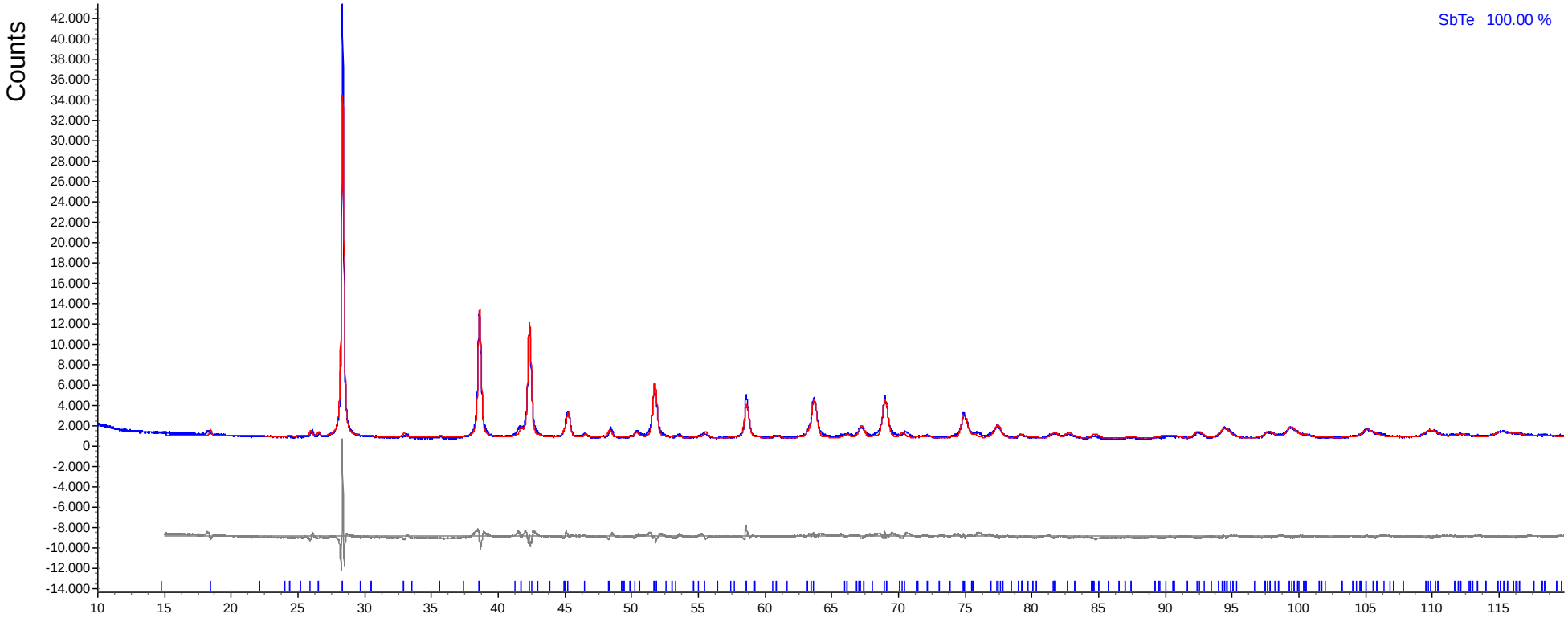

Figure 6.19: Calculated powder pattern of sample 1J_p using Rietveld refinement with the structure model of Stasova et al [20].

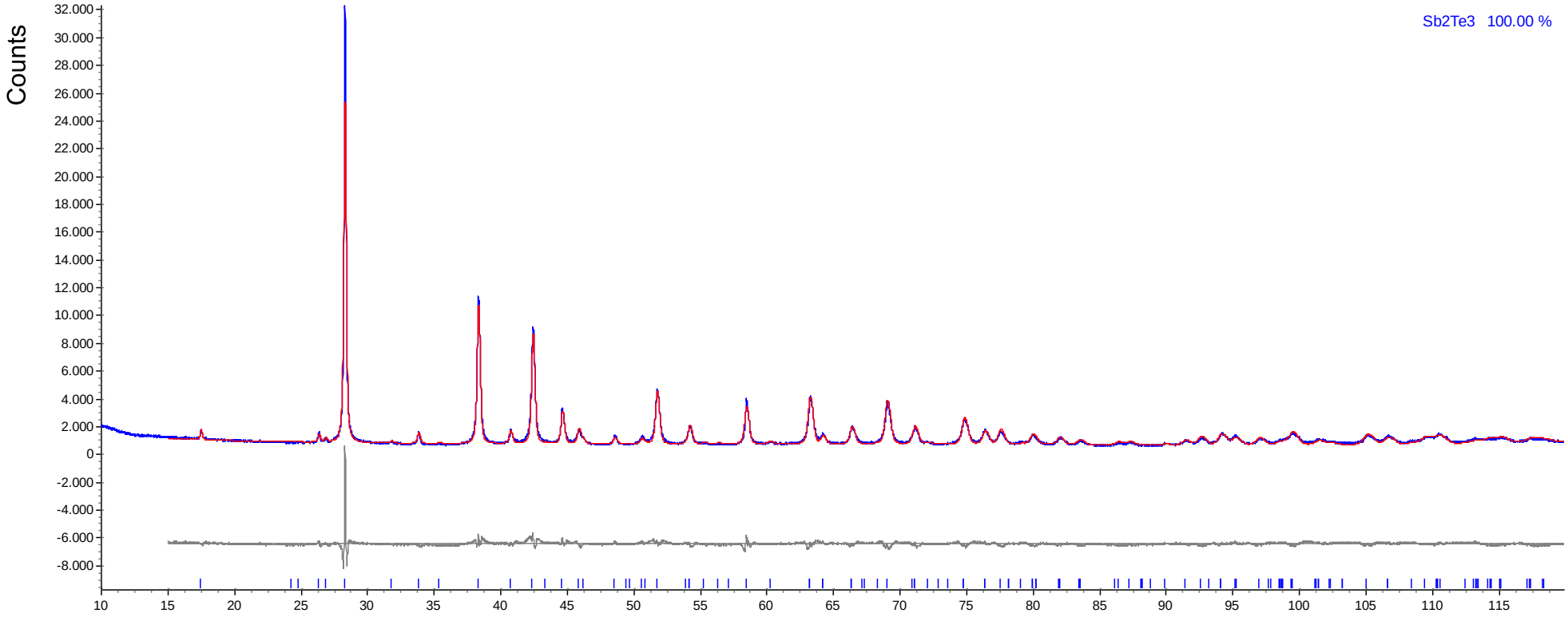

Figure 6.20: Calculated powder pattern of sample 1M_p using Rietveld refinement with the structure model of Belotskii et al. [50].

While evaluating the powder patterns it was tested if some of the structure suggestions also fit into adjacent samples, from a at.% point of few. This hypothesis could never be confirmed, since each structure model was only suitable for the single composition as reported in table 6.4. Even samples, where two phases were measured by the EDX (e.g. 1β_p), the two neighbouring phases, in this example pure Sb and $Sb_{48}Te_9$, could not be confirmed through refinement.

If the powder patterns are compared as a function of composition, arranged with increasing at.% of tellurium one can observe a symmetric drift of reflex positions. This “wandering” reflexes are satellites, which are shifting continuously, but in different directions an d. This behaviour is visualized in figure 6.21.

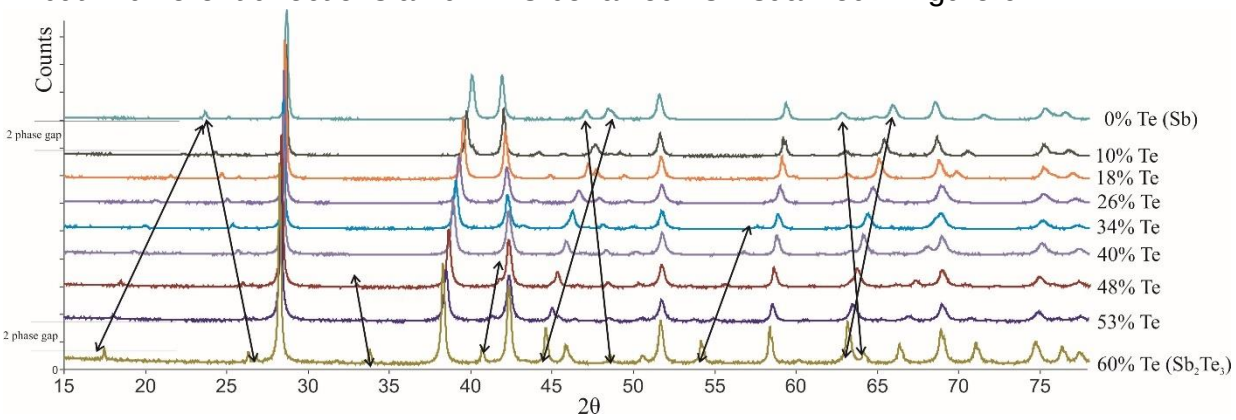

Figure 6.21: Powder patterns of different samples arranged according to their Te content Shifting satellites reflexes are highlighted by arrows.

This strongly drifting satellites could be evidence for an incommensurate modulated behaviour of the extended single-phase field between pure antimony and Sb_2Te_3. It can be assumed that the irrational component of the modulated wavevector (q_j) - as stated in chapter 3.2 it has to be at least one in respect to the main lattice reflections – is in the direction of the c-axis, since all superstructures that have been reported and could be verified in this study are elongated in this direction. These superstructures however, could emerge due to the modulation vector becoming rational for these compositions. Therefore, a final evaluation of the powder pattern was done using the JANA software [46] and applying the structure model used for the Sb-Sn system in the work of Lidin et al. [49].

This model depends on the linear relation between the increasing Sb concentration and the dimension of the incommensurate wavevector ($q = \gamma c^*$). This relation is developed from two end points connected linearly. On the one end pure

Sb, with the value 3/2 and on the other side, the sample with the lowest Sb - concentration Sb_2Te_3, yielding the value 6/5 (see table 6.6).

By verifying the patterns with JANA we were able to obtain the wavevector q_j in respect to the change in composition of the samples. As input we used the above described structural model. For all samples the crystal structure R-3m(00γ) (166) was taken and as basic unit cell. In addition, certain starting values for the lattice parameter had to be used. All samples, which have two phases (1.5alpha, 1.5beta and 2alpha), are refined with additional Sb as the second phase. Also, the lattice parameter a was set to 4.2 Å and the lattice parameter c was set to 5.6 Å. The angles were set according to the trigonal unit cell (90/90/120). Other inputs were a starting value for the q-vector, which was always around 1.4 and the composition of the analyzed sample as description purpose.

Then a first refinement was conducted, which yielded a first fit of the lattice parameter to the powder diffractogram. If the refinement was successful, all prominent reflections were refined but none of the satellites. With the introduction of the wavevector q in the second step the satellites could also be refined until the outcome was satisfactorily. Afterwards Sb-atoms were included to the examination. Only one sort of atoms was used for all samples, which happened in accordance to Lidin et al. [49].

The resulting q-vectors and the refined lattice parameter are listed in table 6.6. An example of a refined powder pattern with JANA is shown in figure 6.22.

a [Å]	c [Å]	γ_q-vector	at.%Te	Phase	R-value [%]
4.308 (±1.72*10^{-4})	5.637 (±3.41*10^{-4})	1.500	0	Sb	15.57
4.302 (±1.78*10^{-4})	5.721 (±3.48*10^{-4})	1.439	6	2 phase field	16.00
4.302 (±1.69*10^{-4})	5.711 (±3.53*10^{-4})	1.440	8		14.39
4.301 (±1.11*10^{-4})	5.715 (±2.31*10^{-4})	1.436	10		14.12
4.295 (±0.77*10^{-4})	5.720 (±2.13*10^{-4})	1.425	12		12.34
4.293 (±0.95*10^{-4})	5.742 (±2.01*10^{-4})	1.418	14		11.01
4.291 (±1.08*10^{-4})	5.758 (±2.48*10^{-4})	1.411	16		13.92
4.288 (±0.86*10^{-4})	5.775 (±1.91*10^{-4})	1.400	18		10.95
4.286 (±0.93*10^{-4})	5.791 (±2.03*10^{-4})	1.385	20		11.12
4.282 (±0.62*10^{-4})	5.805 (±1.71*10^{-4})	1.375	22		10.52
4.281 (±1.15*10^{-4})	5.822 (±2.58*10^{-4})	1.365	24		13.16
4.280 (±1.12*10^{-4})	5.839 (±2.52*10^{-4})	1.358	26	Single phase field	10.23
4.278 (±0.86*10^{-4})	5.850 (±2.51*10^{-4})	1.344	28		13.09
4.277 (±1.10*10^{-4})	5.870 (±2.46*10^{-4})	1.338	30		10.32
4.273 (±0.69*10^{-4})	5.887 (±1.03*10^{-4})	1.322	34		9.62
4.270 (±0.56*10^{-4})	5.916 (±1.60*10^{-4})	1.299	38		9.60
4.269 (±0.93*10^{-4})	5.948 (±2.16*10^{-4})	1.280	42		9.84
4.267 (±0.97*10^{-4})	5.980 (±2.06*10^{-4})	1.260	46		9.14
4.266 (±1.06*10^{-4})	5.999 (±2.27*10^{-4})	1.250	50		8.97
4.264 (±1.35*10^{-4})	6.036 (±2.73*10^{-4})	1.229	53		9.01
4.268 (±1.39*10^{-4})	6.091 (±3.15*10^{-4})	1.200	60	Sb_2Te_3	15.44

Table 6.5: Data gathered from JANA refinement regarding the lattice parameter a, c and the wavevector γ_q.

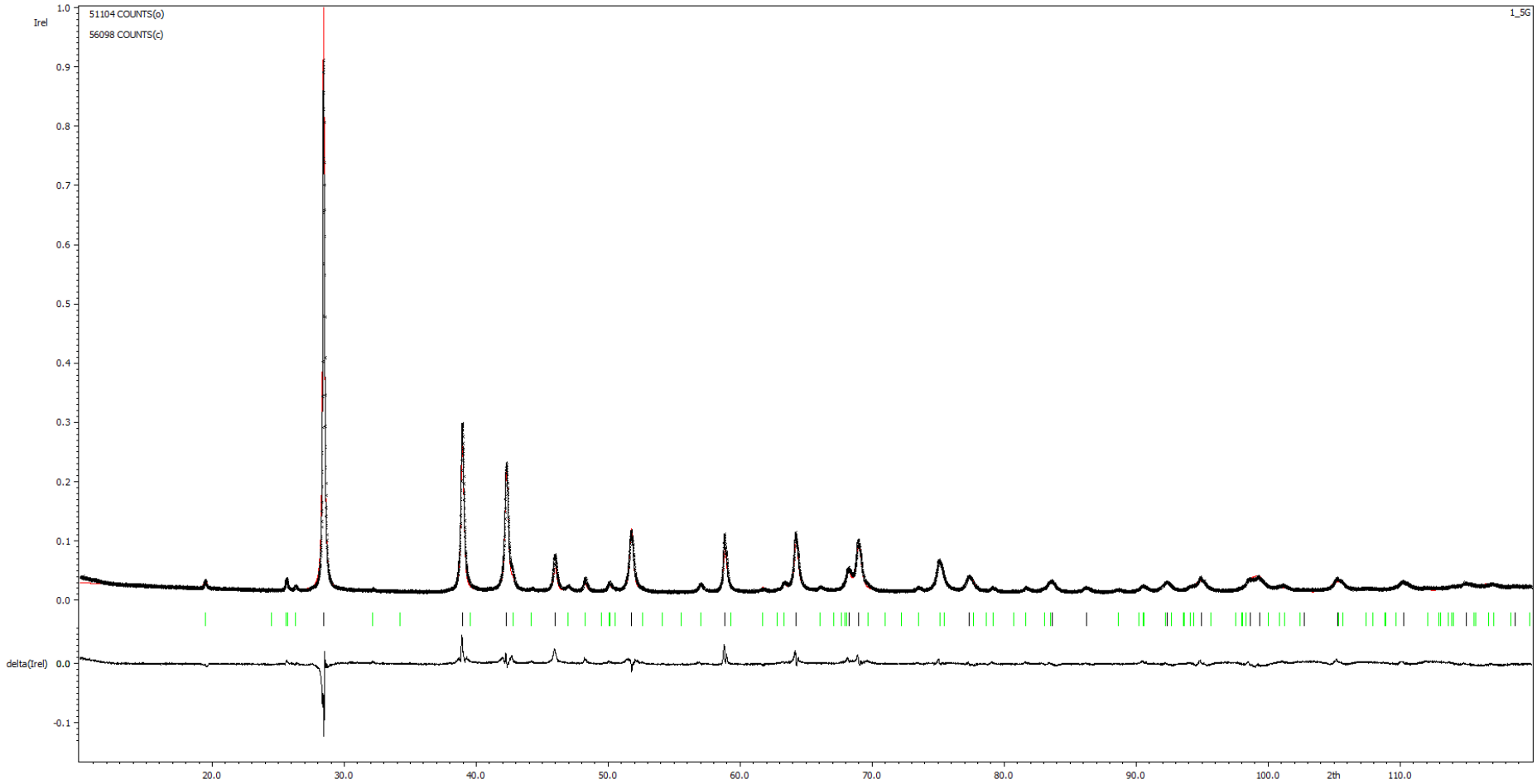

Figure 6.22: JANA refined powder pattern of the powder sample 1G_p, which yield a very good match between refinement and pattern.

As seen in the table with increasing amount of tellurium we have a decrease of the lattice parameter a and of the wavevector q and an increase of the parameter c. The plots of all three parameters can be found in figures 6.23 and 6.24.

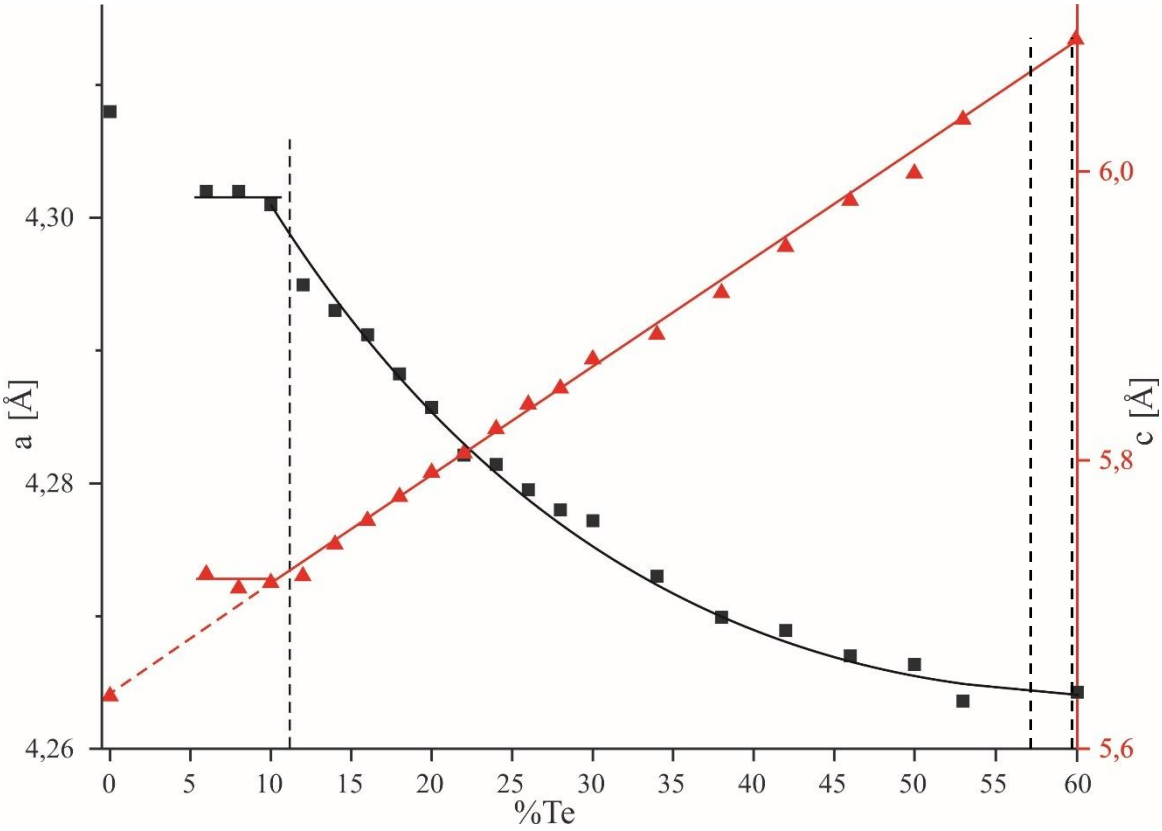

Figure 6.23: Behavior of the lattice parameter a and c in respect to the composition after evaluation with the JANA software. Dashed lines indicate 2-phase fields (see table 6.4).

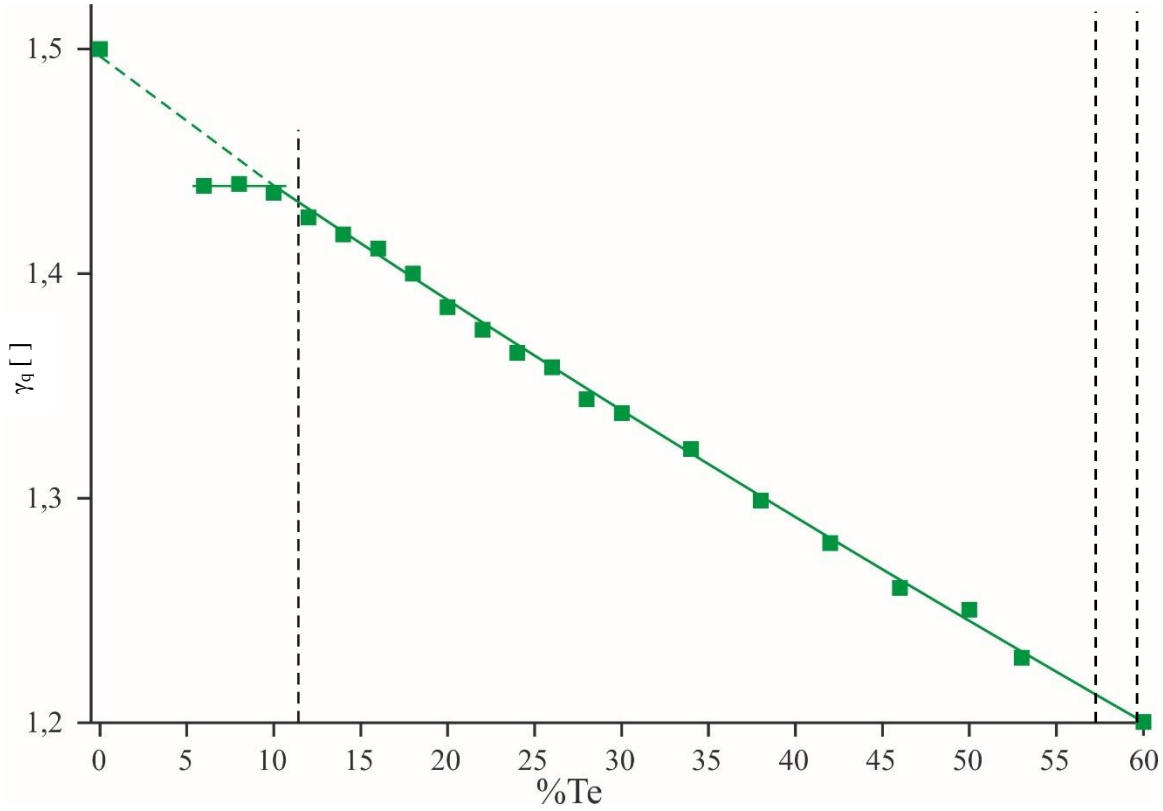

Figure 6.25: Behavior of the q vector in comparison with the composition of each sample obtained through evaluation with JANA. Dashed lines indicate 2-phase fields (see table 6.4).

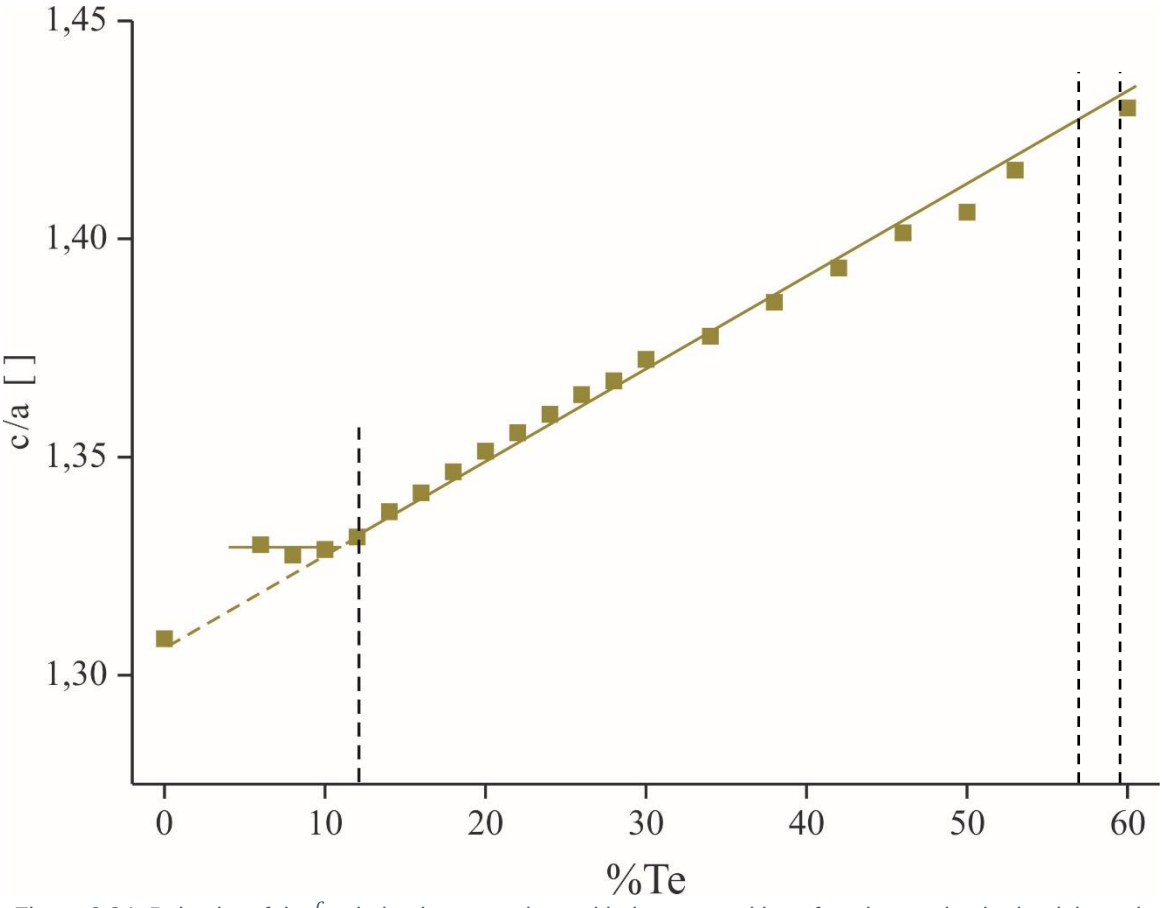

Figure 6.24: Behavior of the $\frac{c}{a}$ relation in comparison with the composition of each sample obtained through evaluation with JANA. Dashed lines indicate 2-phase fields (see table 6.4).

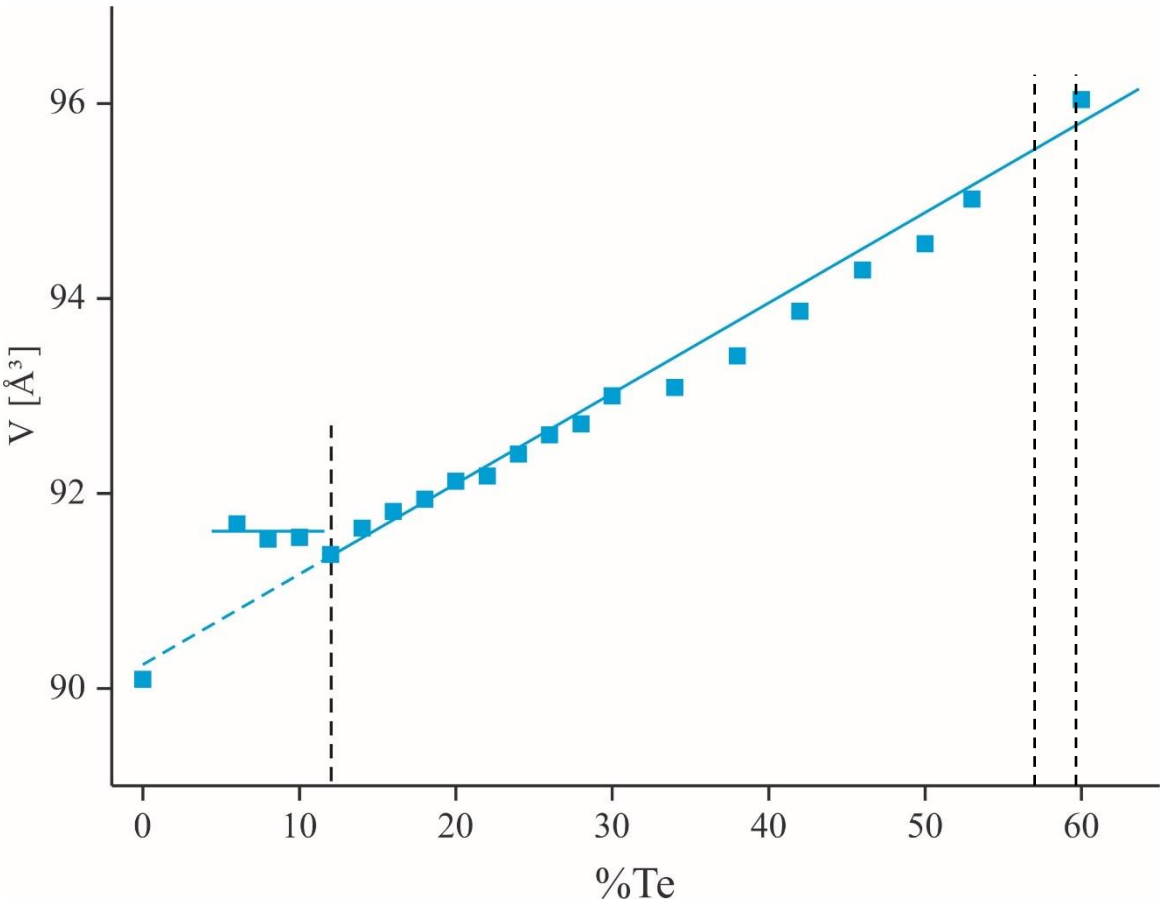

Figure 6.26: Behavior of the unit cell volume in comparison with the composition of each sample obtained through evaluation with JANA. Dashed lines indicate 2-phase fields (see table 6.4).

Figure 6.24 shows a linear relation between the composition regime and the wavevector. This is also true for the lattice parameter c (see figure 6.23). Figure 6.25 (ratio a/c vs. at.% Te) and 6.26 (unit cell volume vs at.% Te) also show a linear behaviour throughout the single phase field.This also stands in harmony with the results of Lidin et al., where there was a linear connection between the wavevector and the concentration of Sn was found [49]. For the two-phase field, all refined parameter were found to be constant, which is due to the reason that there are always the same two distinct composition types present, which would be pure Sb and a compound containing 11.5 at.% Te.

For some compositions the q-parameter yields a rational number, e.g. 1.4, which is 5/7, for 18 at.% Te. It is exactly this sample, which contains a refine able superstructure, namely Sb_4Te. Also the sample with 22 at.% Te yields a rational number (11/8, which is 1,375), so there should be a structure anticipated, however it could not be refined in this work.

With all those results it can be concluded that the γ-phase is indeed incommensurate modulated, while having commensurable modulated structures throughout the system.

6.3 Suggesting a new phase diagram

Based upon all gathered data of the homogeneous samples a new phase diagram suggestion can be made in this thesis. The diagram proposal can be seen

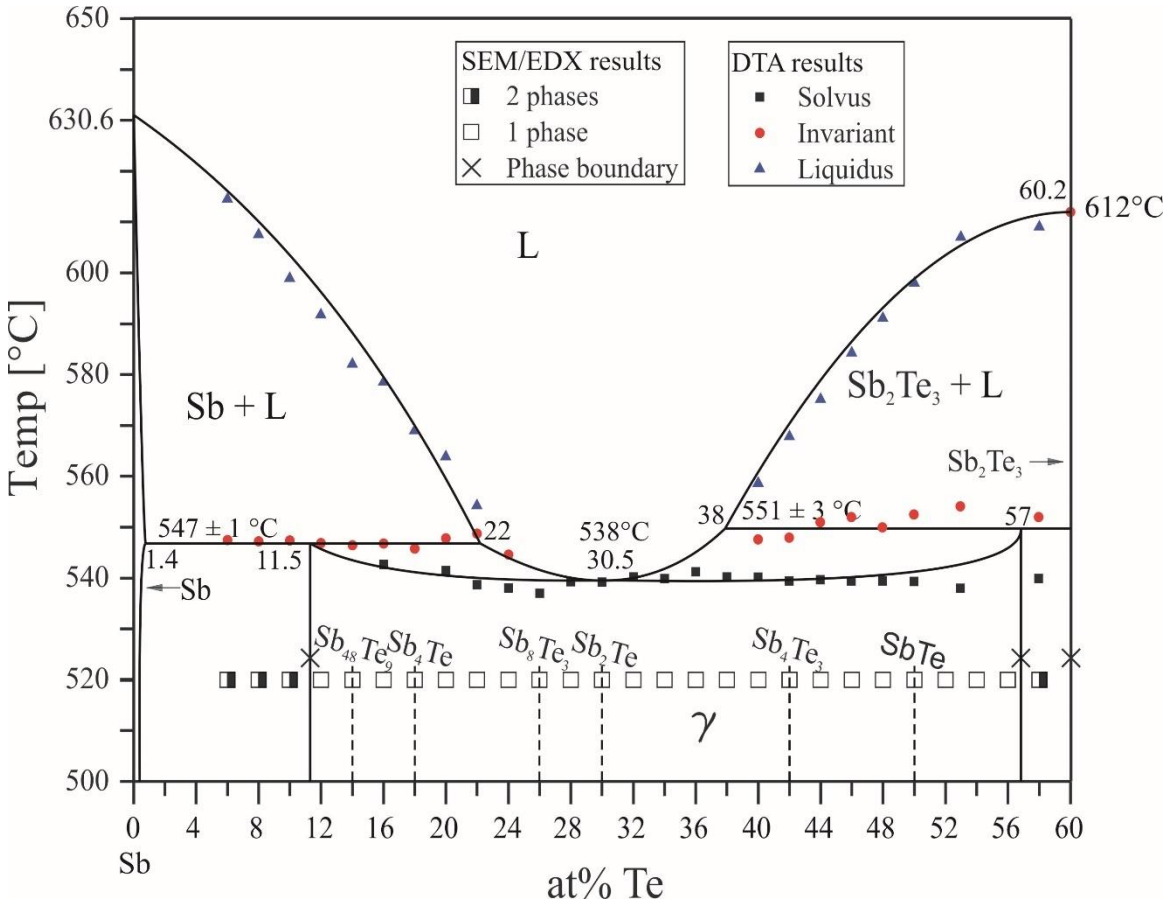

Figure 6.27: Suggestion of a new phase diagram based on the new findings in this thesis.

in figure 6.24. There are major changes made in comparison to parts of the existing literature even if there is partial overlapping (e.g.: homologue series of structures) [12, 22, 23]. The main difference between the suggested diagram and diagrams from previous work is that it is assumed in this thesis that only one intermediate single-phase field - γ - exists between antimony and Sb_2Te_3. This can be concluded from SEM/EPMA measurements, where all samples between 12 and 55 at.% Te were single-phase.

The phase γ has a range from 11.5 to 57 at.% Te and contains several commensurate superstructures besides being incommensurate modulated. Since only one intermediate phase is assumed, only one peritectic reaction on each side of the congruent melting point exists.

All reactions occurring in the system are illustrated in table 6.6. Phase reactions marked with a [*] are assumed based on the literature given in chapter 3, since the main attention in this thesis was on the part of the system between pure Sb and 60 at% Te.

Reaction	Composition of the respective phases [at.% Te]			Temperature [°C]	Reaction type
L ↔ Sb		0		630.6	Melting
L + (Sb) ↔ γ	22.0	1.4*	11.5	547.0 ±1	Peritectic
L ↔ γ	30.5	30.5		538.0	Congruent
L + Sb_2Te_3 ↔ γ	38.0	60.0	57.0	551 ±3	Peritectic
L ↔ Sb_2Te_3 + (Te)*	92.6	60.0	100.0	544.35	Eutectic
L ↔ Te*		100.0		449.55	Melting

Table 6.6: Reactions fitting to the suggested phase diagram. [*] is based on literature [12]

Certainly, there has to be much more research to fully understand the reactions taking place around the congruent melting point. Since the temperature differences are very slim differential thermal analysis proves to be very difficult to evaluate.

7. Abstract

Main goal of this thesis was the reinvestigation of the antimony rich part of the Sb-Te system, based upon existing contradicting literature. Phase boundaries between pure Sb, γ, δ and Sb_2Te_3 were observed closely as well as their connecting phase transformation.

Several samples in the range from 6 to 60 at.% Te were investigated utilizing common examination methods including XRD, DTA, SEM/EPMA and optical microscopy. All samples were additionally studied regarding their possible incommensurate modulated characteristic.

With the acquired data from X-ray powder diffraction, it was possible to refine 6 different structures in the γ-phase. Further utilization of the gathered data was possible, while using the JANA software [46], to determine the possibility, whether the γ-phase is incommensurate modulated or not. After evaluating the obtained q_j-vectors it can be noted, that said phase is indeed incommensurate modulated, passing through several commensurate superstructures, 6 of them shown in this thesis. However, it could be possible that there are even more superstructures in this phase, which needs to be determined in subsequent investigations.

Lastly, after evaluation of data from all sources it was possible to suggest a different phase diagram, which differs with the work from Ghosh et al. [12], on which this thesis is based upon. The suggested phase diagram having only one intermediate single-phase field (γ) and slightly different reaction temperatures.

8. Zusammenfassung

Ziel dieser Arbeit war die Untersuchung des antimonreichen Teils des Sb-Te Phasendiagramm, aufgrund Uneinigkeiten der bestehenden Literatur. Hauptaugenmerk wurde hierbei auf die Phasengrenzen zwischen Antimon, den in der Literatur beschriebenen Phasen γ, δ und Sb_2Te_3 gelegt. Des weiteren wurden die Phasenübergänge mit den dazugehörigen Temperaturen geprüft.

Es wurden zahlreiche Proben unterschiedlicher Zusammensetzung zwischen 6 und 60 at.% Te vorbereitet und mithilfe von Standarduntersuchungsmethoden wie XRD, DTA, SEM/EPMA und optische Mikroskopie, untersucht. Alle Proben wurden zusätzlich auf eine mögliche Inkommensurabilität der zugrundeliegenden Phase(n) untersucht.

Es war möglich, mithilfe der Daten der Röntgenpulverdiffraktometrie 6 unterschiedliche Strukturen in der γ-Phase zu verfeinern. Eine weitere Möglichkeit die gewonnen Röntgendaten zu nutzen, war die Untersuchung auf Inkommensurabilität, mithilfe der Software JANA [46]. Nach Auswertung der erhaltenen γ_q-Vektoren kann zusammengefasst werden, dass zwar eine Inkommensurabilität besteht, diese allerdings durch mehrere kommensurable Überstrukturen verläuft, von denen 6 hier verfeinert wurden. Es liegt allerdings nahe, dass noch mehr solcher Überstrukturen in dieser Phase existieren, was durch folgende Untersuchungen überprüft werden könnte.

Abschließend konnte, basierend auf allen Daten, ein Vorschlag für ein neues Phasendiagramm in dieser Arbeit vorgestellt werden. Dieses Diagramm unterscheidet sich sehr von jenem von Ghosh et al. [12], auf dem diese Arbeit aufbaut. Das vorgeschlagene Phasendiagramm hat zum Unterschied nur ein Einphasenfeld (γ) und außerdem unterschiedliche Reaktionstemperaturen.

9. References

1. Greenwood, N. N.; Earnshaw, A., *Chemistry of the Elements* (2nd ed.)., Butterworth-Heinemann., pp. 581–582, (1997).

2. Yong Tae, K., Seong-Il K., *Comparison of thermal stabilities between Ge-Sb-Te and In-Sb-Te phase change materials*., Appl. Phys. Lett. 103, 121906 (2013).

3. Noboru Y., Eiji O., Kenichi N., Nobuo A., and Masatoshi T., *Rapid-phase transitions of GeTe-Sb2Te3 pseudobinary amorphous thin films for an optical disk memory*., Journal of Applied Physics 69, 2849 (1991).

4. Wang, G., Zhu, X., Wen, J., Chen X., He, K., Wang L., Ma, X., Liu, Y., Dai, X., Fang, Z., Jia, J. and Xue, Q., *Atomically Smooth Ultrathin Films of Topological Insulator Sb2Te3*., Nano Res. 2010, 3(12): 874–880 (2010).

5. Hsieh D., Xia Y., Qian D., Wray L., Meier F., Dil J. H., Osterwalder J., Patthey L., Fedorov A.V., Lin H., Bansil A., Grauer D., Hor Y. S., Cava R. J., and Hasan, M. Z., *Observation of Time-Reversal-Protected Single-Dirac-Cone Topological-Insulator States in Bi_2Te_3 and Sb_2Te_3.,* Phys. Rev. let. 103, 146401 (2009).

6. Wang G., Zhu X., Wen J., Chen X., He K., Wang L., Ma X., Liu Y., Dai X., Fang Z., Jia J., and Xue Q. *Topological insulators in Bi2Se3, Bi2Te3 and Sb2Te3 with a single Dirac cone on the surface*., Nano Res. 3, 874 (2010).

7. Fay H. and Ashley H.E., *Antimony-Tellurium Alloys*., Am. Chem. J., 27, 95-105 (1902).

8. Pélabon H., Thermal Analysis of the Systems Antimony-Tellurium and Selenium-Antimony. *Compt. Rend., 142,* 207-210 (1906).

9. Lukas H. L., Fries S. G., Sundman B., *Computational Thermodynamics – The Calphad Method*, Cambridge University Press (2007).

10. Eckerlin V.E and Stegherr A., *On the Phases in the Sb-Te System*., Acta Crystallogr., 21, Suppl. 7, A78 (1966), German.

11. Kifune K., Kubota Y., Matsunaga T., and Yamada N., *Extremely long period-stacking structure in the Sb–Te binary system*. Acta Cryst. B 61, 492-497 (2005).

12. Ghosh, G., *The Sb-Te (Antimony-Tellurium) System*., J. Phase Equilib. 15, no. 3, 343-360, (1994).

13. Hollemann, A., Wiberg, E. Wiberg, N., *Lehrbuch der anorganischen Chemie*., 102., stark umgearbeitete und verb. Aufl. / von Nils Wiberg. edn, (Walter de Gruyter, 2007).

14. Riedel, E. and C. Janiak, *Anorganische Chemie mit DVD*. 2007, Walter de Gruyter: Berlin.

15. Villars, P. and L.D. Calvert, *Pearson's handbook of crystallographic data for intermetallic phases*. 2nd ed. 1991, Materials Park, OH: ASM International

16. Antimony < https://www.wolframalpha.com/input/?i=Antimony> (2018).

17. Berger, Lev I., *Semiconductor materials.*, CRC Press, pp. 89–91, (1997).

18. Tellurium <https://www.wolframalpha.com/input/?i=Tellurium> (2018).

19. Imamov R.M., and Semiletov S.A., *Crystal Structure of the Phases in the Systems Bi-Se, Bi-Te and Sb-Te*, Krystallogr., 15(5), 972-978 (1971) in Russian; TR: Sov. Phys. Crystallogr., 15(5), 845-850 (1971).

20. Stasova M.M., *Crystal Slructure of Bismuth Selenides and Antimony and Bismuth Tellurides*, Zh. Strukt. Khim., 8(4), 655-661 (1967) in Russian; TR: J. Struct. Chem. (USSR), 8(4), 584-589 (1967).

21. Stasova M.M., *X-Ray Investigation of Some Bismuth and Antimony Chalcogenides*, Zh. Strukt. Khim., 5(5), 793-794 (1964) in Russian; TR: J. Struc. Chem. (USSR), 5(5), 731-732 (1964).

22. Abrikosov, N. Kh., Poretskaya, L. V. and Ivanova, I. P., *The Antimony-tellurium system*, *Zh. Neorg. Khim.,* 4(11), 2525-2531 (1959) in Russian; TR: *Russ. J. Inorganic Chem.,* 4(11), 1163-1166 (1959).

23. Shelimova, L. E., Karpinskii, O. G., Kretova, M. A., Kosyakov, V. I., Shestakov, V. A., Zemskov, V. S. and Kuznetsov, F. A., *Homologous Series of Layered Tetradymite-like Compounds in the Sb-Te and GeTe-Sb_2Te_3 Systems*, Neorganicheskie Material, 36(8), 928-936 (2000) in Russian; Inorganic Materials, 36(8), 768-775 (2000).

24. Stasova, M.M., *Crystal Structures of Bismuth Selenides and Antimony and Bismuth Tellurides*, Extended Abstract of Cand. Sci. (Chem.) Dissertation, Moscow: Moscow Inst. of Fine Chemical Technology, (1967).

25. Imamov, R.M. and Semiletov, S.A., *Crystal Structures of Bi-Se, Bi-Te, Sb-Te Phases*, Kristallografiya*,* 15(5),97-2-978 (1970).

26. Brown, A., Lewis, B., The Systems Bismuth-Tellurium and Antimony-Tellurium and the synthesis of the minerals hedleyite and wehrlite., J. Phys. Chem. Solids, 23, 1597-1604 (1962).

27. Hansen, M. and Anderko, K., *Constitution of Binary Alloys, 339,* 1177. McGraw-Hill, New York (1958).

28. Kim, W. and Chao, G. Y., *Phase relations in the Pt-Sb-Te system*, Canadian Mineral., 28, 675-685 (1990).

29. Kifune K., Fujita T., Tachizawa, T., Kubota, Y., Yamada, N. and Matsunaga, T., *Crystal structures of X-phase in the Sb–Te binary alloy system*, Cryst. Res. Technol., 48(11), 1011-1021 (2013).

30. Donnay, J. D. H., *Morphologie des cristaux de calaverite. Ann. Soc. Geol. Belg.* B55, 222–230 (1935).

31. Korekawa, M., *Theorie der Satellitenreflexe,* Habilitationsschrift der Ludwig-Maximilian Universität München, Germany (1967).

32. Janssen, T., Janner, A., Looijenga-Vos, A. and de Wolff, P. M., *Inkommensurate and commensurate modulated structures*, International Tables for Crystallography Volume C, 8.9.1.1, 907-908 (2006).

33. Campbell, F. C., *Phase Diagrams: Understanding the Basics,* (ASM International, 2012).

34. Hillert, M., *Phase equilibria, phase diagrams and phase transformations: their thermodynamic basis*, 2nd edn, (Cambridge University Press, 2008).

35. Massa, W., *Kristallstrukturbestimmung*, Vol. 7 (Vieweg + Teubner Verlag, 2011).

36. Woolfson, M. M., *An introduction to X-ray crystallography*, 2nd edn, (Cambridge University Press, 1997).

37. Hammond, C., *The basics of crystallography and diffraction,* 3rd edn, (Oxford University Press, 2009).

38. Allmann, R. and Kern, A., *Röntgen-Pulverdiffraktometrie Rechnergestützte Auswertung, Phasenanalyse und Strukturbestimmung*. 2. korr. und erw. Aufl. edn, (Springer, 2003).

39. Brandon, D. G. and Kaplan, W. D., *Microstructural characterization of materials,* 2nd edn, (John Wiley Sons, 2008).

40. Vander Voort, G. F. in *ASM Handbook* Vol. 9, 1184 (ASM International, Materials Park, Ohio, 2004).

41. Predel, B., Hoch, M. J. R. and Pool, M., *Phase diagrams and heterogeneous equilibria: a practical introduction*, (Springer, 2004).

42. Murphy, D. B. and Davidson, M. W., *Fundamentals of light microscopy and electronic imaging*. 2nd edn, (Wiley-Blackwell, 2013).

43. Reed, S. J. B., *Electron microprobe analysis and scanning electron microscopy in geology,* 2nd edn, (Cambridge University Press, 2005).

44. Goldstein, J., *Scanning electron microscopy and x-ray microanalysis,* 3rd edn, (Kluwer Academic/Plenum Publishers, 2003).

45. Zhao, J. C., *Methods for phase diagram determination,* (Elsevier, 2007).

46. Petricek, V., Dusek, M. and Palatinus, L., *Crystallographic Computing System JANA2006: General features*, Z. Kristallogr. 229(5), 345-352 (2014).

47. Puchegger, S., Fakultätszentrum für Nanostrukturforschung; Zeiss Supra 55 VP, <http://nanozentrum.univie.ac.at/gerae/zeiss-supra-55-vp/> (2018).

48. Poudeu, P.F.P., Kanatzidis, M.G., *Design in solid state chemistry based on phase homologies. Sb_4Te_3 and Sb_8Te_9 as new members of the series $(Sb_2Te_3)_m{\cdot}(Sb_2)_n$*, Chemical Communications (Cambridge), 2672-2674 (2005).

49. Lidin S., Christensen, J., Jansson, K., Fredrickson, D., Withers, R., Norén, L., and Schmid, S., *Incommensurate Stistaite – Order made to Order*, Inorg. Chem., 48, 5497-5503 (2009).

50. Belotskii D.P., Babyuk P.F., *The In_2Te_3-Sb_2Te_3 system*, Inorg. Mat., (translated from Neorganicheskie Materialy), 6, 505-507 (1970).